Sediment flux measurement at high concentration based on image analysis

Master's Thesis

Sediment flux measurement at high concentration based on image analysis

September 2014

Graduate School of Marine Science and Technology

Tokyo University of Marine Science and Technology

Master's Course of Marine System Engineering

Wu Lianhui

ABSTRACT

Sediment transport in the coastal environment usually occurs under the combination influence of various hydrodynamic processes. It is important to understand these sediment transport processes, for the purpose of coastal defense, for the design of various types of coastal structures, for the solution of sedimentation problems in the near shore zone. Hence, an accurate estimation of sediment flux is of great importance for understanding sediment transport processes under numerous conditions. While despite its importance, there are few effective instruments and techniques that can quantify sediment flux precisely with high temporal and spatial resolution.

In this study, an improved sediment flux measurement system was developed. It consists of two image-based techniques respectively for sediment concentration and transport velocity measurement. Motion images of sediment particles in target flow are recorded by a high-speed camera at a large frame rate with an electro luminescence sheet as a backlight source. The stroboscope is synchronized with the camera through a time delay generator at half of the frame rate. Thus, normal (backlight only) and strobe-illuminated images are alternatively obtained at half of the camera frame rate. Sediment concentration is estimated from the normal images using pre-calibrated relationship on the basis of the Lambert-Beer law. By applying PIV technique to each set of the normal and strobe-illuminated motion images, two different results of sediment particle velocities are obtained. Sediment flux then can be figured up by multiplying the concentration and velocity at respective locations.

Verification tests show that the improved system is successful in measuring sediment transport of high concentration. It is confirmed that highly concentrated sediment denser than 190 g/l in the path length of 1.5cm could be measured accurately, far more than existing measurement system. Limitation in the factor of light attenuation of the existing system has been broken through in the improved system.

Laboratory experiment of sediment transport in the swash zone under dam-break waves was carried out. 20 dam-break bores were generated in total to investigate the hydrodynamics of a moveable fine sand beach under discrete swash event. A laser distance measurement system was used for determining the bed profile variation. The improved sediment flux measurement system was applied for study the sediment transport process. Temporal and spatial distribution of sediment concentrations, transport velocities and sediment transport rates were obtained by the light extinction method and a special designed MATLAB-based PIV program, including multiple pass cross-correlation interrogation algorism, parabolic peak fit method, normalized local outlier detection technique and PCHIP interpolation process.

It is found that the wave down rush period is much longer than the up wash and sand bed close to the toe is eroded significantly while the further bed is accreted. Variation of the initial profile slowed down and turned out to be not proportional to the number of dam-break waves but it did not achieve equilibrium even until 20 waves scouring. Vertical distribution of horizontal velocity shows that the velocity profiles have a typical shape of the turbulent flow close to the bed and the velocity gradients decayed during the wave run up while increased along with the rush down and it decreased again in the final stage of wave reverse. Sediment concentration and transport rate decreased

with the increase of elevation. Differences among elevations were extremely different and it is expected to be further illustrated. Sediment transport close to the bottom is regarded as the dominant role of bed profile change.

ACKNOWLEDGEMENT

CONTENTS

Chapter1. Introduction

1.1Overview of sediment transport

Approximately 44% of the world's population lives within 150 km of coastal line (Syvitski et al., 2005). Due to the continually growing of large cities, harbors, port facilities, waterways, railroads, more and more of the world's people are migrating to the coastal regions.

Coastal regions have major implications for human beings, while it is also facing with many natural and human-induced environmental problems. One of the most important issues is the coastal morphologies. Changes of the coastal morphologies are of great importance not only to the residents but also to the nature eco-systems in the coastal regions. The strip of land along the seashore can be classified into rocky coasts and sandy beaches according to the land-forming materials (Kiyoshi et al., 1988). Coastal morphologies are highly dynamic. The behavior of coastal may be studied over a range of scales, both temporal and spatial, which vary from grain to grain interactions over seconds to the scale of shoreline evolution over centuries (Masselink and Kroon, 2009). The beach form can be reshaped by earthquake, tsunami, storm events drastically in several minutes, also may be transformed by tides and waves gradually in a time scale of years or even centuries. In addition, it is associated with coastal engineering constructions closely.

Fig. 1-1 illustrates the behavior of coastal morphological changes in the near shore zone. All of the elements impact on each other intensively and cannot be analyzed isolated.

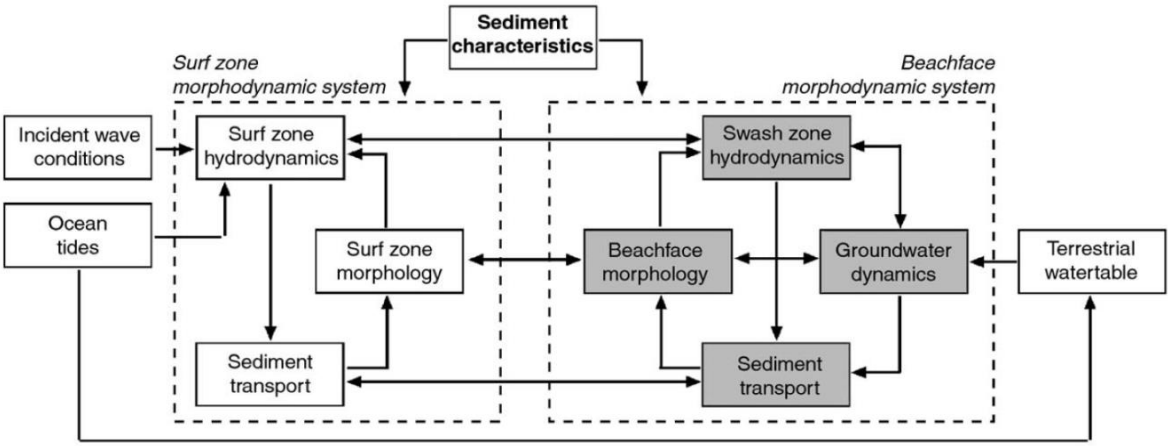

Figure 1-1 Nearshore zone morphodynamic system (Masselink and Puleb, 2006)

One important factor of the coastal morphologies is sediment transport. It is defined as the movement of solid particles caused by the gravity acting on the particles and the force of moving fluid imparted. It occurs in natural systems such as rivers, lakes, oceans, where the particles can be sand, gravel, mud or clay. The ability of a particle to move is then related to shear stresses, frictional forces, water depth, and specific weight.

Sediment transport in the near shore region is usually divided into cross-shore and long shore by direction. Cross-shore transport is mainly produced by wave orbital motion, whereas long shore transport is primarily associated with wave-induced long shore currents. The long shore transport is considered as a chief mechanism for long term of beach evolution, while the cross-shore transport is related to the short term changes.

Fig. 1-2 illustrates the transition of sediment transport mode in the littoral zone. There are several classification methods of sediment transport mode in the littoral zone. A generally acceptable classification method is dividing sediment transport modes into wash load, suspended load and bed load, based on the transport mechanism. The wash load consists of very fine particles which are transported by water and normally they are

not represented in the bed. Therefore, it is usually neglected when we calculate or simulate the total sediment discharge. There are no precise definitions of suspended load and bed load as there is no clear boundary between them. Roughly speaking, the suspended load is the sediment that is moving without continuous contact with the bed, and the sediment particles follow the motion fluid very well. The bed load is defined as the sediment that is in more or less continuous contact with the bed during the transport. In the bed load transport mode, inter-particle forces play an important role. Sediment transport in the coastal region makes an important contribution to the morphologic change and it is essential to understand the process well.

1.2 Overview of sediment flux measurement

Sediment transport is a complex process and development of suitable methods for sediment transport measurement that contribute to understanding the process is a still-evolving science. Generally speaking, sediment transport may be envisioned either as a rate or as a concentration. In respect of sediment transport rate, sediment flux is used for defining the transport rate, which has a unit of mass per unit time or volume per unit time (e.g., kg/s or m^3/s). In which, sediment concentration and transport velocities are usually measured simultaneously for describing the sediment transport rate. Sediment flux and the concentration and velocity have the relationship as follows:

$$Q = \iint c u_s dydz \tag{1-1}$$

where Q is sediment flux, c is sediment concentration, u_s is sediment transport velocity. Once the sediment concentration and transport velocities are measured, sediment flux can be calculated through the above equation.

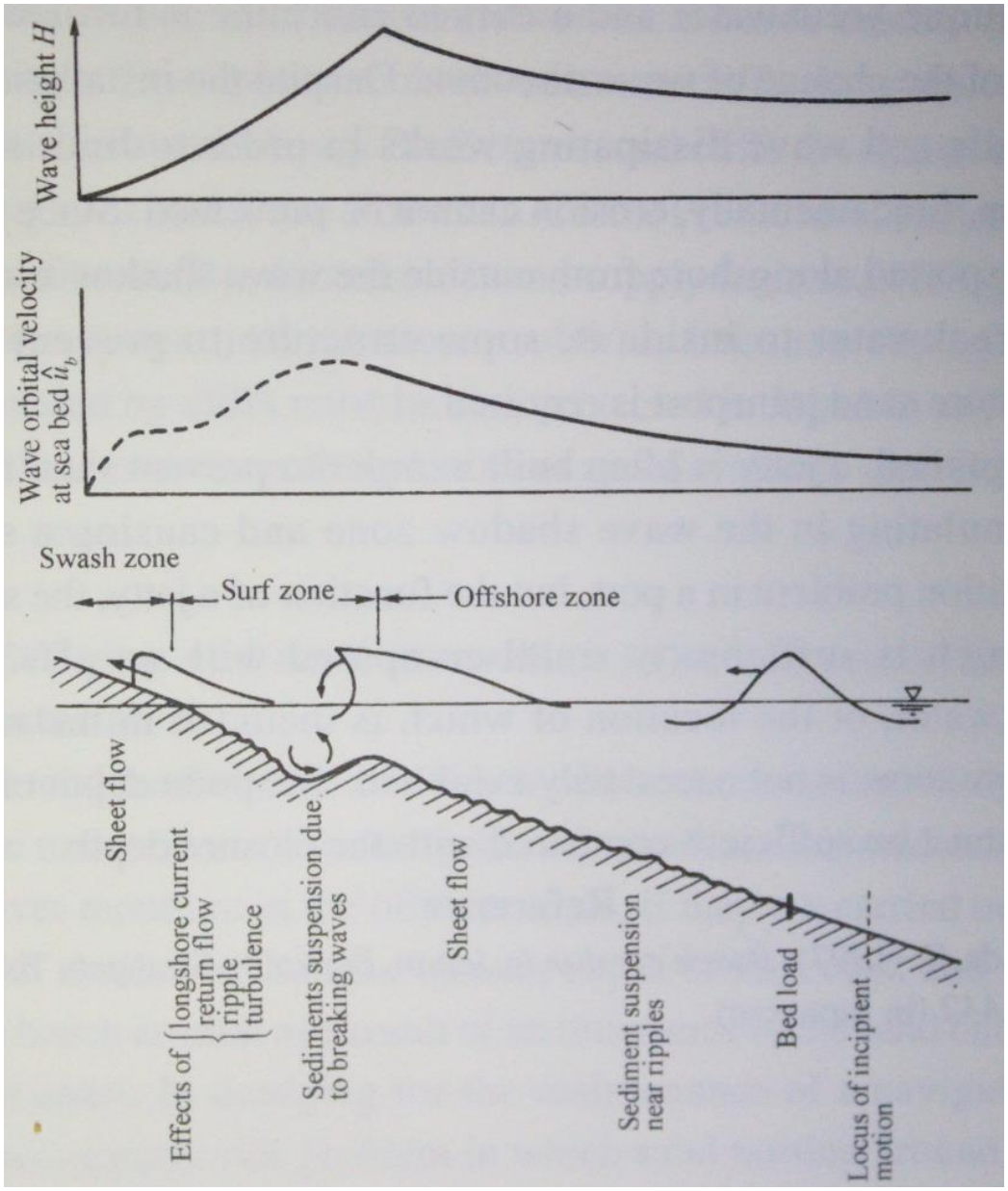

Figure 1-2 Cross-shore sediment transport modes (Asano, T. etc., 2000)

Various kinds of measurement instruments have been developed for both laboratory experiments and field survey in order to provide insight into the sediment transport process. The first method developed is manual sampling of suspended sediment and analyses of characteristics of the material collected. Grab sampling, pump sampling, isokinetic sampling and other manual sampling methods are still popular in field

surveys nowadays (e.g. Bothner and Valentine, 1982; Lewis, 1996; Dark and Allen, 2005; Yang, 2008). Generally, these instruments are reliable and accurate and remain a reference for calibration of other methods, while temporal resolution of these instruments is usually limited by available manpower or instrument operating time. And these instruments are flow intrusive and laboratory analysis is necessary to determine sediment concentration and particle characteristics.

Over the last three decades, the application of acoustics (Hanes et al., 1988; Hay and Sheng, 1992; Thorne and Hardcastle, 1993, 1995, 1997; Thosteson and Hanes, 1998) and optics (Downing et al., 1981; Ludwig and Hanes, 1990; Sternberg et al., 1991; Bunt et al., 1999; Agrawal and Pottsmith, 1993, 1994, 2000) to the measurement of sediment transport, especially small scale sediment process have been gaining increasing acceptance. Because some of the acoustics and optics measurement instruments have the potential to measure non-intrusively, with high temporal and spatial resolution, profiles of suspended sediment size and concentration, profiles of flow, and the bed form morphology. Thorne and Hanes (2006) gave an intensive review of acoustic measurement, including the principle, calibration and illustrations. And a series of experiments, both in coastal zone and laboratory flumes have been conducted to simultaneously and non-intrusively measure seabed morphology, the suspended sediment particle size, concentration profile, and the velocity profile with required resolution, based on acoustic instruments such as Acoustic or Ultrasonic Sand Transport Meter (AUSTM), Acoustic Sand Transport Monitor (ASTM), UHCM-instrument (e.g. Libicki et al., 1989; Lynch et al., 1991; Traykovski., 1999). In respect of optical measurement methods, optical backscatter sensor (OBS) is the most widespread

instrument. Since the first OBS introduced by Downing et al. (1981), many OBSs have been developed to estimate sediment concentration and fluid turbidity for studying of sediment transport. Various OBSs are desired for satisfying different research conditions, while the principles of all OBSs are same. Downing (2006) discussed the features of OBSs in detail, including the principle, advantages and shortages. Optical Laser diffraction point sensor (LISST) is another optic based instruments. Various LISSTs are commercially available for measure the particle size and concentration of suspended sediments. Although numerous acoustic and optical measurement instruments have been developed to study the sediment transport, and they contribute us to understand the sediment process indeed, there are still many factors influence the acoustic and optical measurements. One critical problem is that both of the acoustic and optical instruments are strong particle size dependent, which brings significant troubles for the calibration and measurement (Ludwig and Hanes, 1990; Conner and Devisser, 1992). For homogeneous sediments, most acoustic and optical sensors response to varying concentrations of them is nearly linear, whereas in reality, sediments are usually mixture of mud, clay, sand and rocks. In these cases, acoustic and optical sensors are likely to give large errors. In addition, backscattering signal do not response to the small changes of concentration at high and low particle concentrations in regard to some sensors.

Other measurement instruments such as nuclear sensor (Berke and Racozai, 1981) and conductivity sensor (O'Donoghue and Wright) have also been developed for studying sediment transport, while these instruments are not widely used in laboratory study and

field survey for some reasons. A conclusion of various measurement instruments, including operating principles, advantages and disadvantages are given in Table 1-1.

Recent years, visualization techniques are appealing to more and more scientists and engineers with their obvious merits. High-speed cameras are utilized in various sediment transport experiments and numerous post-processing methods have been developed for data analysis (e.g. Liu and Sato, 2005; Radice et al., 2006; Shimozono et al., 2013). It is possible to study sediment process without disturbing the target flow as they are virtually non-intrusive techniques, and temporal and spatial distribution of sediment flux can be obtained at high resolution by image techniques, which contributes to the verification and calibration of numerical models very much.

As for sediment transport velocity, few of the above–mentioned instruments are able to measure sediment concentration and particle velocities simultaneously. More commonly, acoustic Doppler velocimeters (ADV), laser Doppler velocimeters/anemometry

Table 1-1 sediment measurement techniques

Technology (1)	Operating principle (2)	Advantages (3)	Disadvantages (4)
Acoustic	Sound backscattered from sediment is used to determine size distribution and concentration.	Good spatial and temporal resolution, measures over wide vertical range, nonintrusive	Backscattered acoustic signal is difficult to translate, signal attenuation at high particle concentration
Bottle sampling	Water-sediment sample is taken isokinetically by submerging container in streamflow and is later analyzed.	Accepted, time-tested technique, allows determination of concentration and size distribution, most other techniques are calibrated against bottle samplers	Poor temporal resolution, flow intrusive, requires laboratory analysis to extract data, requires on-site personnel
Pump sampling	Water-sediment sample is pumped from stream and later analyzed.	Accepted, time-tested technique, allows determination of concentration and size distribution	Poor temporal resolution, intrusive, requires laboratory analysis, does not usually sample isokinetically
Focused beam reflectance	Time of reflection of laser incident on sediment particles is measured.	No particle size dependency, wide particle size and concentration measuring range	Expensive, flow intrusive, point measurement only
Laser diffraction	Refraction angle of laser incident on sediment particles is measured.	No particle-size dependency	Unreliable, expensive, flow intrusive, point measurement only, limited particle-size range
Nuclear	Backscatter or transmission of gamma or X-rays through water-sediment samples is measured.	Low power consumption, wide particle size and concentration measuring range	Low sensitivity, radioactive source decay, regulations, flow intrusive, point measurement only
Optical	Backscatter or transmission of visible or infrared light through water-sediment sample is measured.	Simple, good temporal resolution, allows remote deployment and data logging, relatively inexpensive	Exhibits strong particle-size dependency, flow intrusive, point measurement only, instrument fouling
Remote spectral reflectance	Light reflected and scattered from body of water is remotely measured.	Able to measure over broad areas	Poor resolution, poor applicability in fluvial environment, particle-size dependency

(LDV/LDA), ultrasonic velocity profilers (UVP) and particle image velocimetry (PIV) are employed in sediment transport experiments combined with various sediment concentration measurement instruments to estimate sediment flux (e.g. Dick and Sleath, 1991, 1992; Ribberink and Alsalem, 1995; O'Donoghue and Wright, 2004). Among these velocity instruments, PIV is considered as the most promising method because it is non-intrusive with high temporal and spatial resolution. In addition, ADV and LDV/LDA have more limitations and difficulties compared with PIV. For example, these instruments are usually performed terrible in high sediment concentration conditions.

In summary, all of the measurement methods have their own specialties and shortages. Careful consideration is necessary according to different research objectives and complex experimental conditions before selecting suitable instruments for studying sediment transport.

1.3 Motivation and objective of the study

Up to now, numerous laboratory experiments have been conducted to measure sediment concentration and transport velocities on the basis of the above-mentioned instruments, while there are few simple instruments can simultaneously measure concentration and velocities with high spatial and temporal resolution. Shimozono et al. (2008, 2013), Masame (2013) developed an image-based technique that is cable of measuring sediment concentration and transport velocities simultaneously. A light extinction method was used to measure sediment concentration, and PIV analysis was employed to measure transport velocities. It can measure sediment flux with an error of no more than 10% when the sediment concentration is not very high, while in dense conditions, they

found that the disappearance of traceable pattern due to the rising concentration made the PIV analysis break down. Therefore, the system could only measure sediment flux in a certain concentration range. The current study is on the basis of their work. In this study, we focus on extending the existing measurement system for sediment transport of much higher concentration and try to apply the improved measurement system to flume experiments.

1.4 Outline of the thesis

General introduction of sediment transport and measurement methods for sediment transport are given in chapter 1. Merit and demerit of various velocity and concentration measurement methods for sediment transport are compared in this chapter.

Improved image-based sediment flux measurement system is presented in chapter 2. Measuring principles of the improved system are descripted in detail and measuring range of sediment concentration is discussed based on amounts of results in different calibration conditions.

Chapter 3 presents the verification tests for the sediment flux measurement system. It includes the determination of the measuring limit of the previous system and validation tests of the improved system.

Laboratory study of sediment transport in the swash zone under dam-break waves is introduced in chapter 4. Measurements of the experiments were on the basis of the improved system.

Conclusions of present study and some future plans are given in chapter 5.

Chapter2. Improved image-based sediment flux measurement system

2.1 Introduction

Shimozono et al. (2012) developed the original image-based sediment flux measurement system. Sketch of the measurement system is given in Fig. 2-1. An electro luminescence sheet (EL-Sheet) was set in the target flow as a backlight source to illuminate the sediment particles, which is a planar lighting device with a brightness of 300 cd/m2 and central wavelength of 510-520 nm. The EL-Sheet acts like a stiff paper and can be placed in water without disturbing the target flow significantly, as its thickness is only about 0.5mm. Motion images of sediment particles in target flow were recorded by a high-speed camera, and sediment concentration and transport velocities were measured from the recorded images. Two image-based techniques respectively for concentration and velocity measurements were employed in the measurement system. Sediment concentration is estimated form a pre-calibrated relationship with light attenuation through water volume containing sediment particles. Transport velocities were

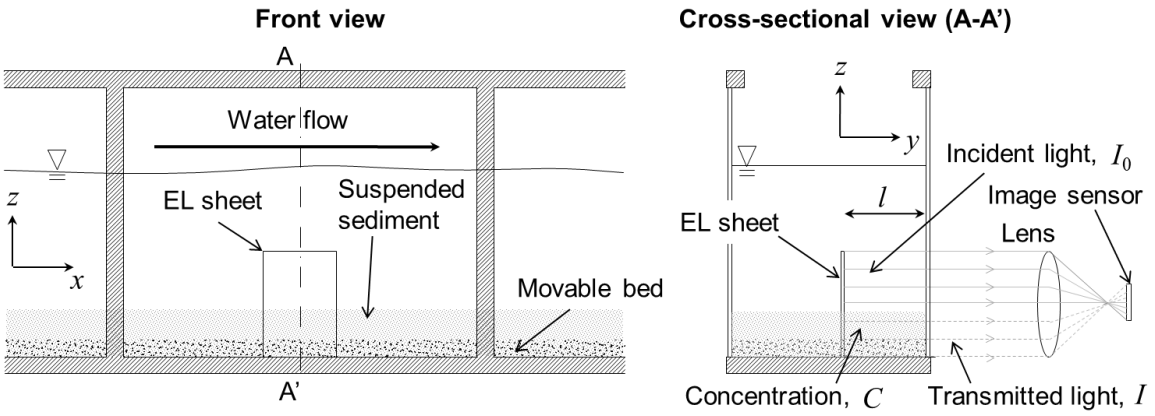

Figure 2-1 Sketch of the image-based measurement system (Shimozono et al., 2013)

simultaneously measured by PIV technique in the same image. Thus, spatial distribution of sediment fluxes could be obtained by simply multiplying the sediment concentration and transport velocity at respective locations. For low sediment concentrations, the system performed well with a measuring error no more than 10%. While they found that when the concentration is high, the rising concentration will make the traceable pattern disappear from the recorded images, which is essential for PIV analysis. Therefore, sediment fluxes cannot be successfully measured in those cases.

In order to overcome the difficulties of velocity analysis in the previous system, several new instruments were applied in the improved measurement system. Fig. 2-2 illuminates the side view of the improved system. Similar with the previous measurement system, there is an electro EL-Sheet set in the target flow as a backlight source. A high-speed CMOS camera (IDT Inc., M3) is employed to record motion images of sediment movement with a maximum resolution of 1280×1024 pixels. As mentioned above, PIV analysis will break down caused by the disappearance of the traceable patterns in the recorded images when the concentration is high. The reason is that light from the EL-sheet cannot pass through the flow due to a huge amount of sediment particles in that case. Therefore, a stroboscope (Nissin Electronic CO., Ltd., JX612, 0.3J/F, exposure time is 15-30μs, maximum frequency is 200Hz) is set in front of the experimental flume as an additional light source to illuminate the highly concentrated sediments. Synchronized by a time delay generator (Stanford Research Systems, Inc., DG645), the stroboscope is controlled to give out light at half of the camera frequency. Thus, normal (backlight only) and strobo-illuminated images are alternatively obtained at the same frequency. Examples of instantaneous normal and

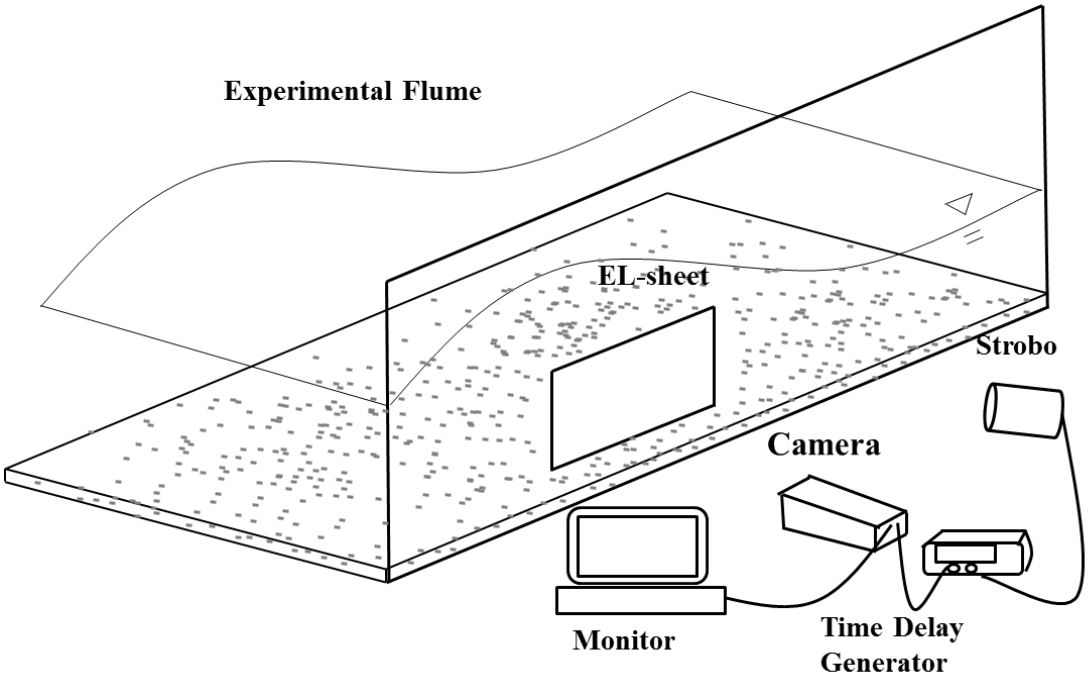

Figure 2-2 Side view of the improved image-based measurement system

strobo-illuminated images are shown in Fig. 2-3. Normal images can be used for concentration measurement and strobe-illuminated images are for velocity analysis.

Once sediment concentration and transport velocity can be obtained simultaneously, sediment flux then can be deduced from Eq. 1-1. In short, this chapter will describe the image-based concentration and velocity measurement techniques in detail.

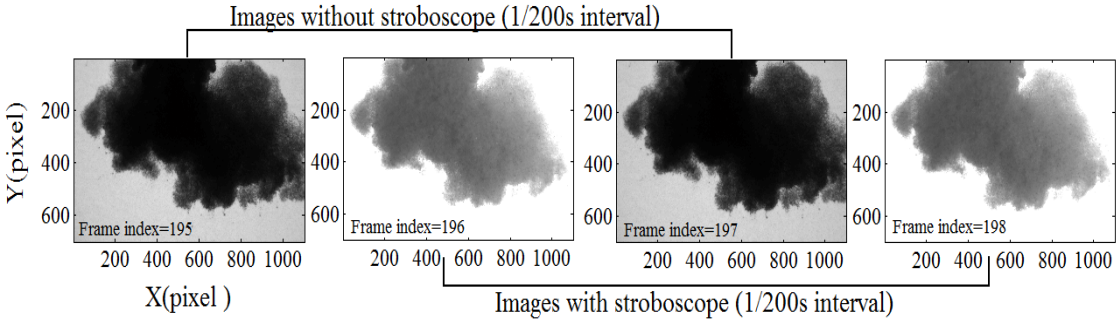

Figure 2-3 Instantaneous images obtained by the improved measurement

2.2 Sediment concentration measurement

2.2.1 Principle of concentration measurement

The current study utilizes a light extinction method developed by Shimozono et al. (2008) to measure the sediment concentration on the basis of the Beer-Lambert law. The law states that there is a logarithmic dependence between the light transmissivity and the product of the absorption coefficient of the substance, and the path length. It can be written as follows:

$$A = \sigma_{ext} l \tag{2-1}$$

$$A = -\log \frac{I}{I_0} \tag{2-2}$$

$$\sigma_{ext} = \frac{\pi d_s^2}{4} N Q_{ext} \tag{2-3}$$

where A is the light attenuation. σ_{ext} is the attenuation coefficient. l is the path length that stands for the distance the light travels through the material. I_0 and I are initial light intensity of the EL-sheet and detected light intensity after the presence of sediment particles respectively. d_s is the particle diameter and N is the particle number density. Q_{ext} is the absorption coefficient related to the substance the light travel through.

The particle number density can be transformed into mass concentration as:

$$N = \frac{6c}{\rho \pi d_s^3} \tag{2-4}$$

where c, ρ, d_s are concentration, sediment density and particle diameter separately. Then (2-1) can be written as follows by substituting Eq. 2-3 and Eq. 2-4 into the equation,

$$A = \frac{3}{2} Q_{ext} \frac{cl}{\rho d_s} \tag{2-5}$$

Since light attenuation can be obtained from the recorded images, given l, ρ, d_s, sediment concentration can be deduced from the light attenuation according to Eq. 2-5 if the factor of Q_{ext} could be determined. The schematic diagram of concentration measurement method is shown in Fig. 2-4. Thus, previous calibration is necessary to determine the relationship between the sediment concentration and light attenuation (e.g. the factor of Q_{ext}).

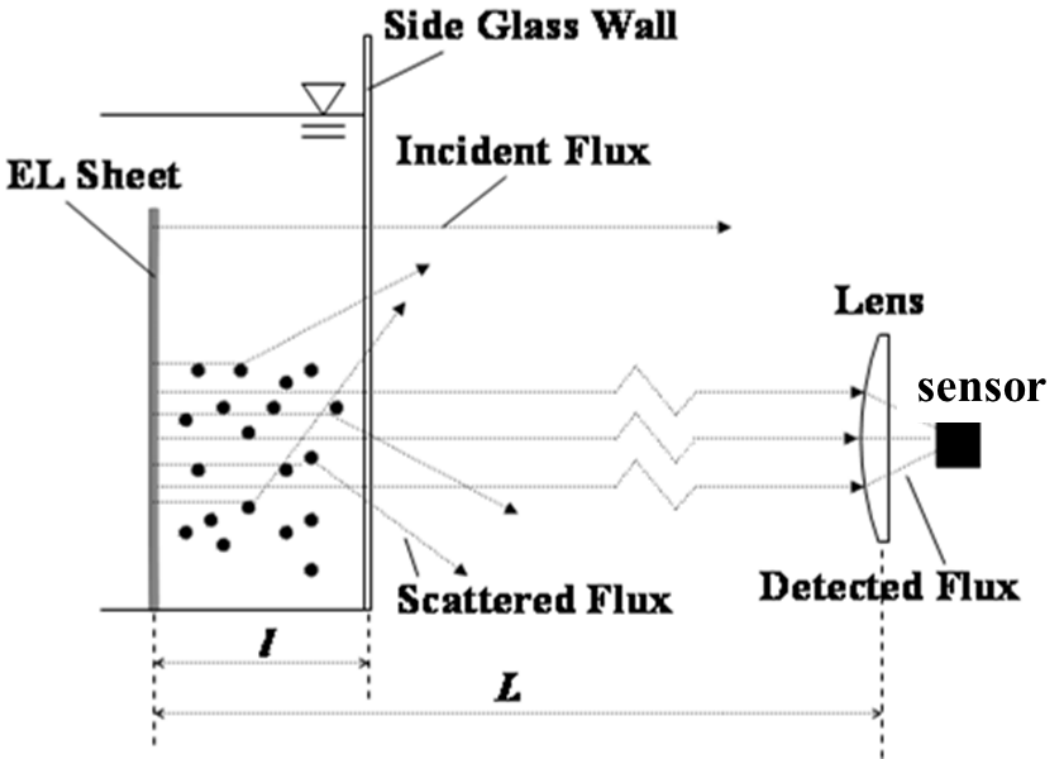

Figure 2-4 Schematic diagram of concentration measurement

2.2.2 Concentration calibration

In current study, a transparent acrylic container filled with precisely known concentration was used for calibration experiment. The setup of calibration experiment is illuminated in Fig. 2-5. There was an EL-sheet setting in front of the high-speed

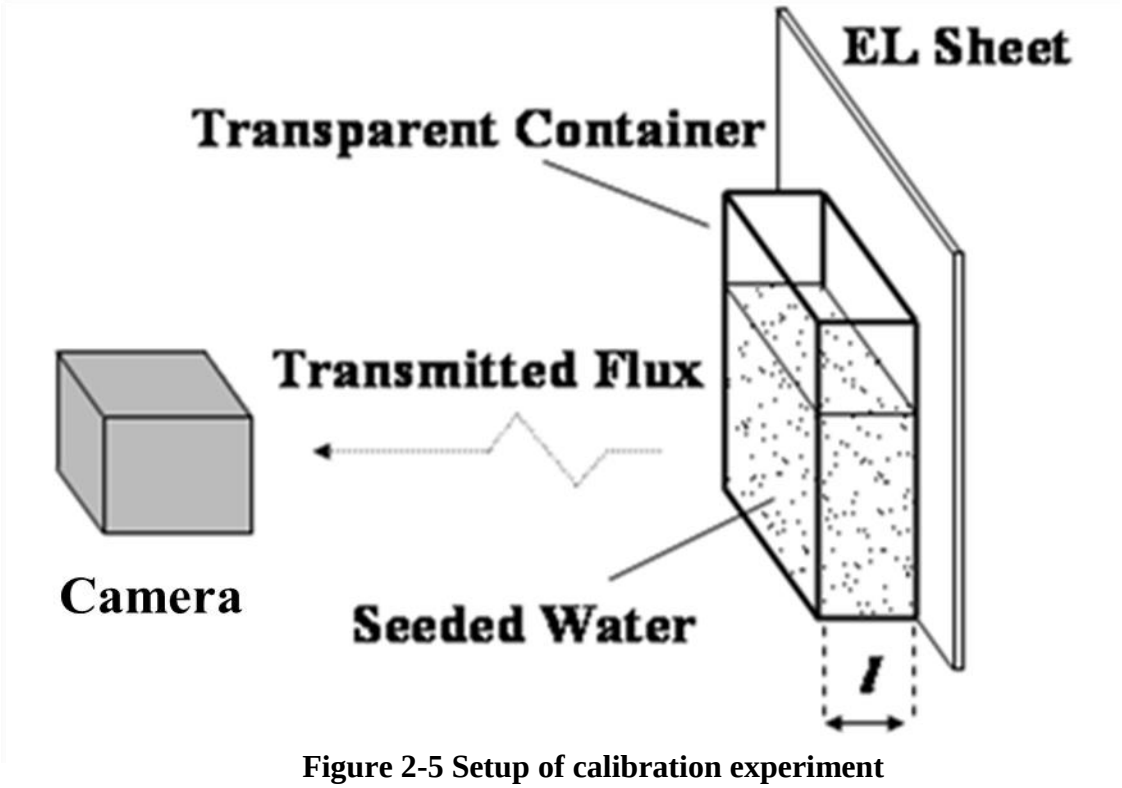

Figure 2-5 Setup of calibration experiment

camera. For each time, the container was filled with a certain amount of silica sand with a median diameter of 0.16 mm, and it was shaken by hands to uniform the concentration throughout it and immediately placed in front of the EL-sheet. After putting in front of the EL-sheet, sediment particles started settling and air bubbles went up swiftly, while the concentration still remained uniform and kept constant for a while in the middle layer of the container (Fig. 2-6). Meanwhile, the high-speed camera was triggered to record the process, and then the transmission intensity could be evaluated from the averaged light intensity over the corresponding part of the recorded image. In order to cover a wide range of concentration, a serious of concentrations were used in the

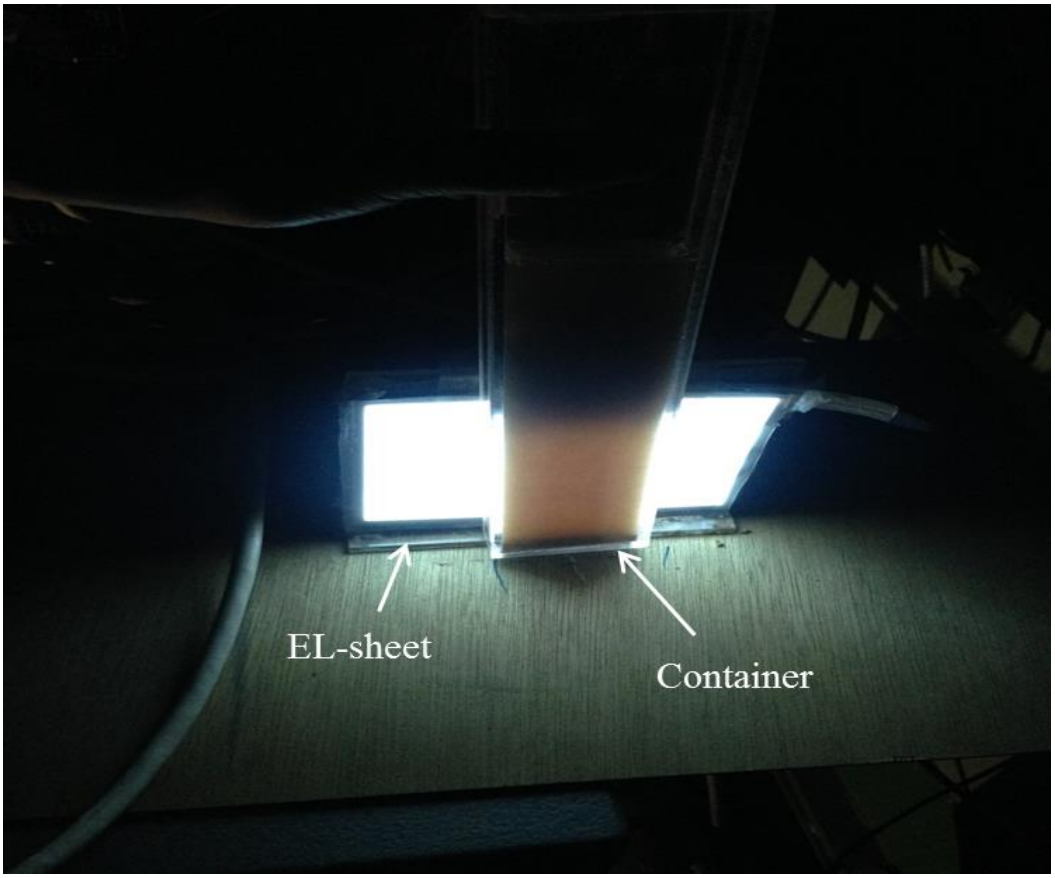

Figure 2-6 Transparent acrylic container used in calibration

calibration. Moreover, different containers with the width (path length) of 1.0 cm, 1.5 cm, 2.0 cm, 3.0 cm, 4.0 cm, 4.5 cm and 5.0 cm were used in the calibration. In each case, the procedure was repeated several times to minimize the accidental error. Detailed calibration conditions are listed in Table 2-1 and example images of different light attenuation are illuminated in Fig. 2-7. Specific calibration results of each path length are shown in Fig. 2-8.

It is easy to find that the relationship between the sediment concentration and light attenuation do not satisfy the Beer-Lambert law strictly. This phenomenon is caused by strong light scattering when the concentration is very high as the silica sand is non-absorptive material. And it becomes obvious accompany with the increase of the path

Table 2-1 Experimental conditions of calibration (g/l)

Container Width (Path Length)	1.0cm	1.5cm	2.0cm	2.5cm	3.0cm	4.0cm	4.5cm	5.0cm
Case1	0	0	0	0	0	0	0	0
Case2	1	1	1	1	1	1	1	1
Case3	2	2	2	2	3	3	2	2
Case4	3	5	5	3	5	5	3	5
Case5	4	10	10	4	10	10	4	10
Case6	5	20	20	5	15	15	5	20
Case7	10	30	30	10	20	25	7	30
Case8	20	50	40	15	30	35	10	40
Case9	30	75	50	20	40	45	15	50
Case10	50	100	75	25	60	55	20	75
Case11	80	125	100	30	80	70	30	100
Case12	100	150	125	40	100	85	40	150
Case13	150	175	150	50	120	100	50	200
Case14	200	200	200	60	150	150	60	300
Case15	250	225	250	80	200	200	80	
Case16	300	250	300	100	300	300	100	
Case17	350	300	350	150			150	
Case18	400	350		200			200	
Case19	500			300			300	

length. In the case of path length equals to 1.0 cm, the relationship between concentration and light attenuation can keep linear until the concentration exceeds 300 g/l, while in the case of path length equals to 5.0 cm, the linearity can only maintain below 40 g/l in the factor of concentration. Thus, suitable path length should be selected according to the practical experimental conditions and light attenuation can be converted into concentration on the basis of these calibration results.

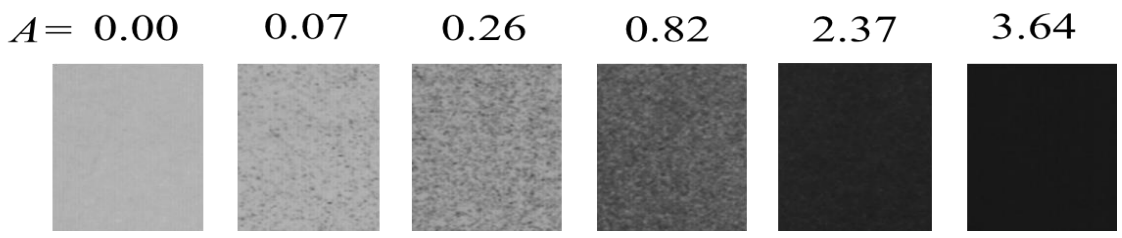

Figure 2-7 Example images of different light attenuation

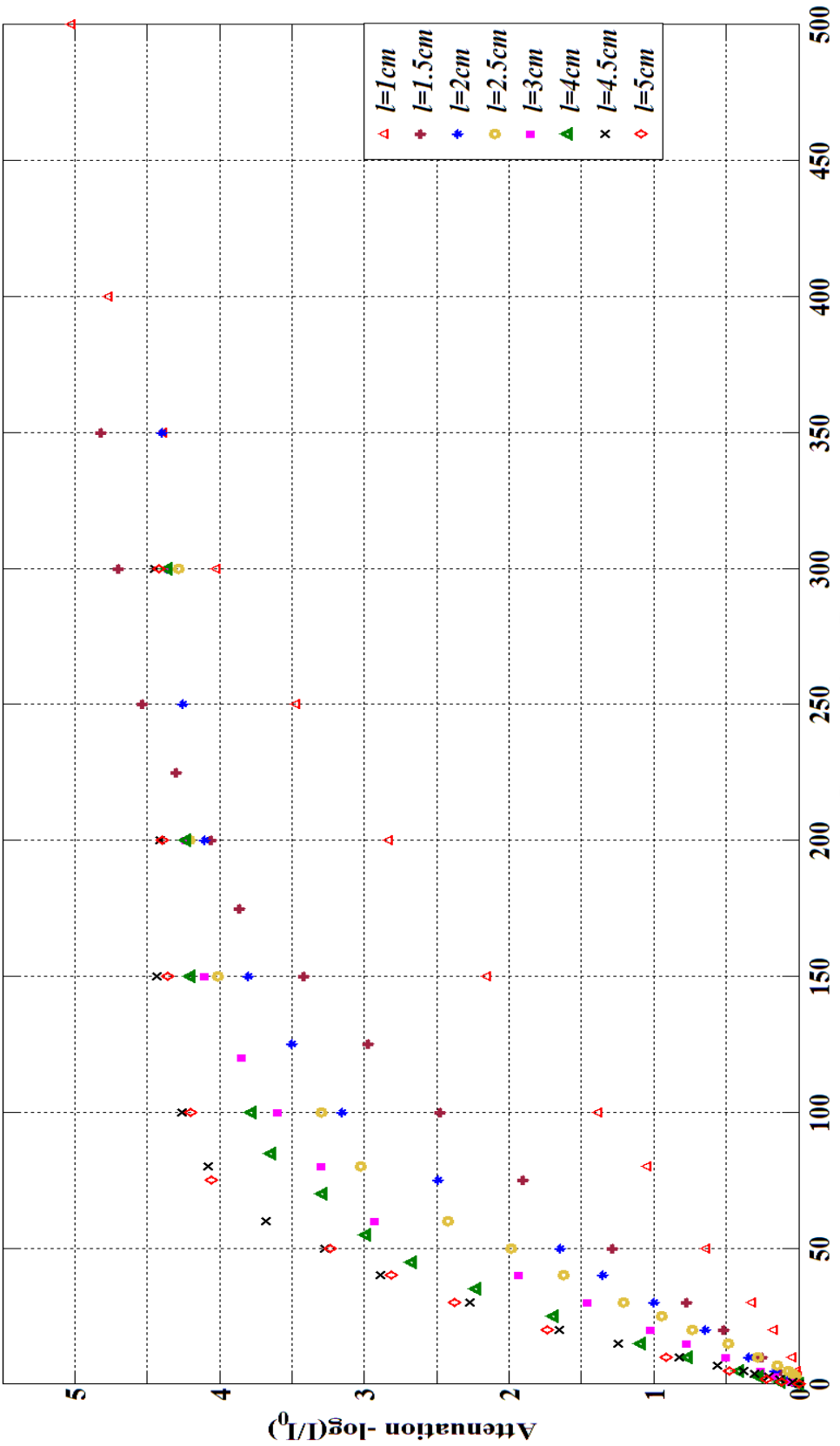

Figure 2-8 Calibration results for different path length

What should be noted is that each calibration curve is conducted on different experimental conditions, including the camera aperture size, shutter speed, the distance between the high-speed camera and EL-sheet. And for current concentration measurement method, measurement range can be adjusted according to different research objectives. For example, if we enlarge the camera aperture size, than higher concentration range can be measureable but low concentration band will be missed. Table 2-2 and Fig. 2-9 illuminate the comparison between large and small aperture sizes in the path length of 2.5 and 4.5 cm. It is easy to find that two calibration curves are completely different. Therefore, when we employ these calibration curves in laboratory experiments, the experimental conditions should be same with the calibration conditions in principle. However, making the camera setting same with the calibration conditions will limit the flexibility of instruments setup as some laboratory experiments need to adjust the aperture size and shut speed of the high-speed camera depending on realistic conditions. On account of serious tests, we find that it is not necessary to make sure that the laboratory experimental conditions and the calibration conditions are completely same. There are two sufficient conditions to ensure that calibration curve can be applied in laboratory experiment. One is that the distance from the high-speed camera to the EL-sheet must be same between the calibration condition and laboratory experimental condition. Another one is that the initial light intensity of the EL-sheet must be same between the calibration condition and laboratory experimental condition, which can be achieved by adjust the aperture size and shut speed. However, for the conditions of large aperture size, the camera is overexposure and the initial light intensity maintains in 255 (maximum value of light intensity) despite the increasing of concentration in a certain range (e.g. calibration result of large aperture size in the path

Table 2-2 Difference of light attenuation between small and large aperture size

Path length	Aperture size										
2.5cm	small	concentration (g/l)	0	1	2	3	4	5	7	10	15	20
		light attenuation	0.00	0.00	0.01	0.02	0.04	0.07	0.14	0.28	0.49	0.74
	large	concentration (g/l)	0	2	4	10	20	30	40	50	60	70
		light attenuation	0.00	0.00	0.00	0.00	0.00	0.18	0.65	1.04	1.41	1.80
	small	concentration (g/l)	25	30	40	50	60	80	100	150	200	300
		light attenuation	0.95	1.21	1.62	1.99	2.42	3.03	3.29	3.86	4.21	4.29
	large	concentration (g/l)	80	110	130	150	170	190	220	250	300	350
		light attenuation	2.08	2.83	3.19	3.43	3.61	3.75	3.83	3.87	3.86	3.97
4.5cm	small	concentration (g/l)	0	1	2	3	4	5	7	10	15	20
		light attenuation	0.00	0.04	0.13	0.21	0.30	0.38	0.56	0.82	1.25	1.65
	large	concentration (g/l)	0	1	5	8	10	20	30	40	50	60
		light attenuation	0.00	0.00	0.00	0.00	0.00	0.78	1.50	2.10	2.69	3.09
	small	concentration (g/l)	25	30	40	50	60	80	100	150	200	300
		light attenuation	1.96	2.27	2.89	3.28	3.68	4.08	4.26	4.44	4.41	4.45
	large	concentration (g/l)	70	80	110	130	150	170	190	220	250	300
		light attenuation	3.41	3.67	3.98	4.06	4.11	4.18	4.21	4.19	4.19	4.23

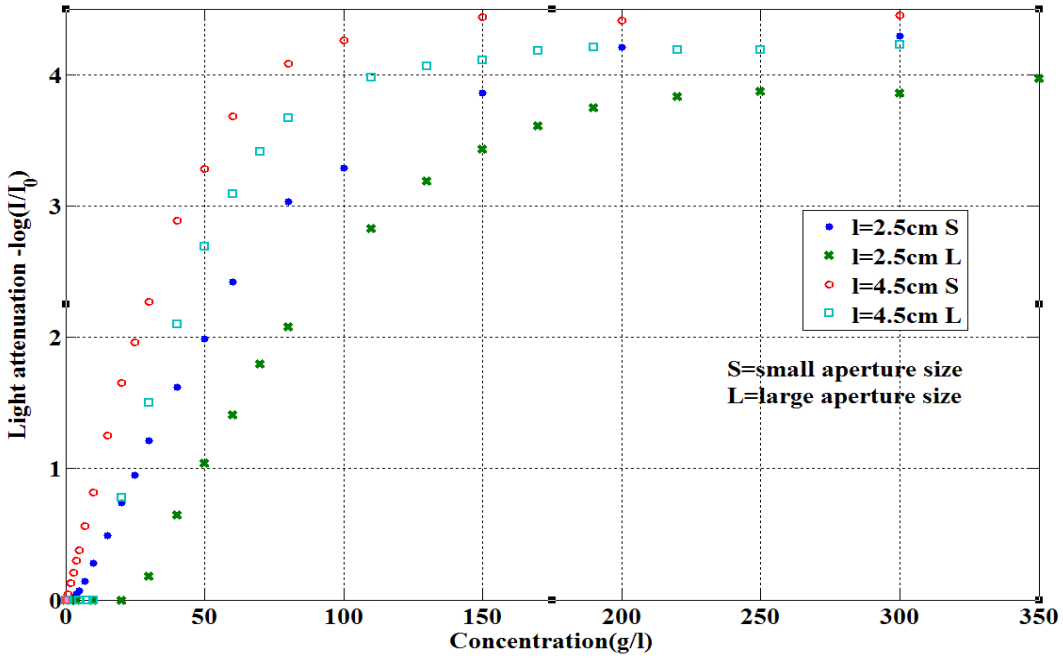

Figure 2-9 Difference of light attenuation between small and large aperture size

length of 2.5cm). In that case, initial light intensity of EL-sheet cannot be used as an indicator, while the transparent container used in calibration experiments can be applied for adjusting the camera aperture size and shut speed. The method is similar with the calibration experiments. After fixing the position of the high-speed camera, the transparent container loading with precisely known concentration of sediment is put in

the experimental location to check the light intensity. Once the light intensity is same with the calibration result under the same concentration by means of different combinations of aperture size and shut speed, the calibration curve is considered can be used in that experimental condition. Thus, the application of these calibration curves become much more flexible and light attenuation can be converted into sediment concentration based on the calibration results.

2.3 Transport velocity measurement

2.3.1 Principle of particle image velocimetry

In current study, particle image velocimetry (PIV) is employed to measure the transport velocity of sediment. In the following, the basic features of this measurement technique will be described briefly.

The experimental setup of a PIV system typically consists of several subsystems. In most applications tracer particles have to be added to the flow. These particles have to be illuminated in a plane of the flow at least twice within a short time interval. The light scattered by the particles has to be recorded either on a single frame or on a sequence of frames. The displacement of the particle images between the light pulses has to be determined through evaluation of the PIV recordings. In order to be able to handle the great amount of data which can be collected employing the PIV technique, sophisticated post-processing is required (Raffel et al., 2007).

Fig. 2-10 briefly sketches a typical setup for PIV recording in a wind tunnel. Small tracer particles are added to the flow. A plane (light sheet) within the flow is illuminated twice by means of a laser (the time delay between pulses depending on the mean flow

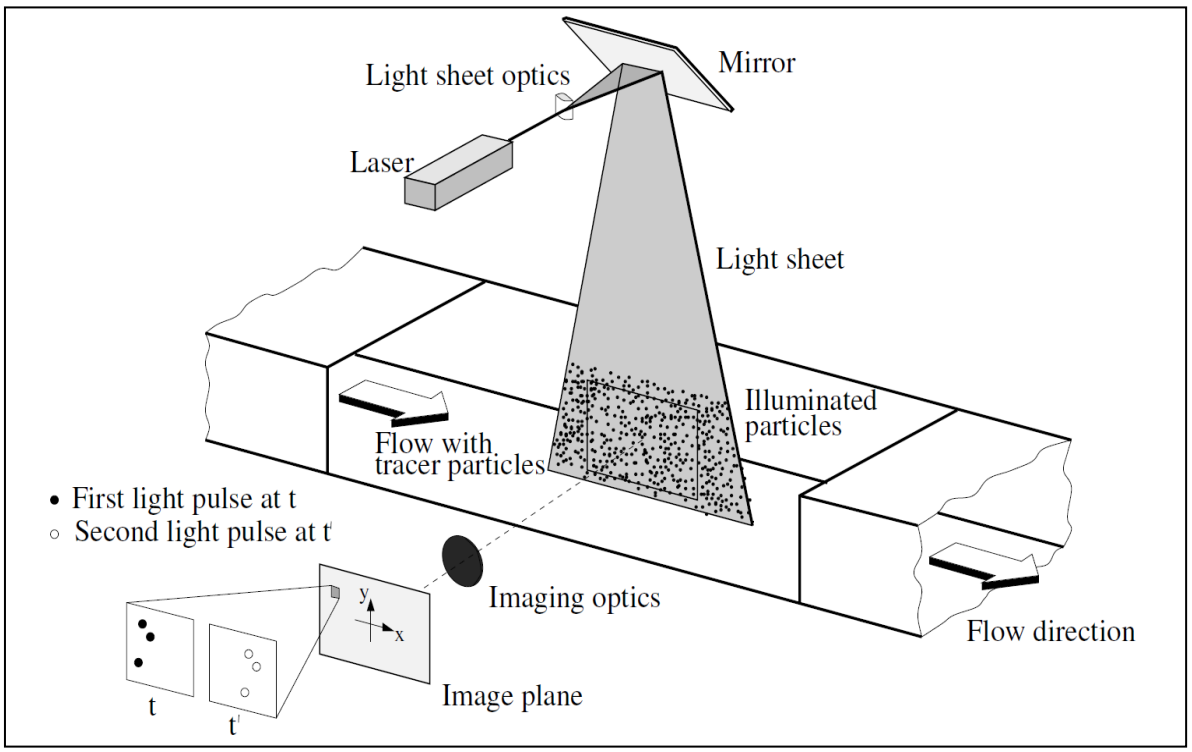

Figure 2-10 Experimental arrangement for particle image velocimetry

velocity and the magnification at imaging). It is assumed that the tracer particles move with local flow velocity between the two illuminations. The light scattered by the tracer particles is recorded via a high quality lens either on a single frame (e.g. on a high-resolution digital or film camera) or on two separate frames on special cross-correlation digital cameras. After development the photo-graphical PIV recording is digitized by means of a scanner. The output of the digital sensor is transferred to the memory of a computer directly.

For evaluation the digital PIV recording is divided in small subareas called "interrogation areas". The local displacement vector for the images of the tracer particles of the first and second illumination is determined for each interrogation area by means of statistical methods (auto- and cross-correlation). It is assumed that all particles

within one interrogation area have moved homogeneously between the two illuminations. The projection of the vector of the local flow velocity into the plane of the light sheet (two-component velocity vector) is calculated taking into account the time delay between the two illuminations and the magnification at imaging.

The process of interrogation is repeated for all interrogation areas of the PIV recording. High-speed recording on charge coupled device (CCD) cameras and complementary metal oxide semiconductor (CMOS) sensors allows for acquisition in the kHz range. The evaluation of one digital PIV recording with several thousand instantaneous velocity vectors (depending on the size of the recording, the interrogation area and processing algorithm) is of the order of a second with standard computers. If data is required at even faster rates for online monitoring of the flow, dedicated software algorithms which perform evaluations of reduced precision within fractions of a second are commercially available.

2.3.2 Velocity evaluation of PIV

From the above description, a summary can be concluded that the PIV is a whole field, non-intrusive, indirect velocity measurement technique that can obtain the velocity information with high accuracy and temporal and spatial resolution. Basic principle of this widely used PIV evaluation method will be introduced in the following.

For a pair of successive images recorded by high-speed cameras, the most we can hope for is to measure the straight-line displacement of the particle images since the curvature information between the recording instances is lost. Further, the seeding density is too homogeneous that it is difficult to match up discrete particles. In some cases the spatial

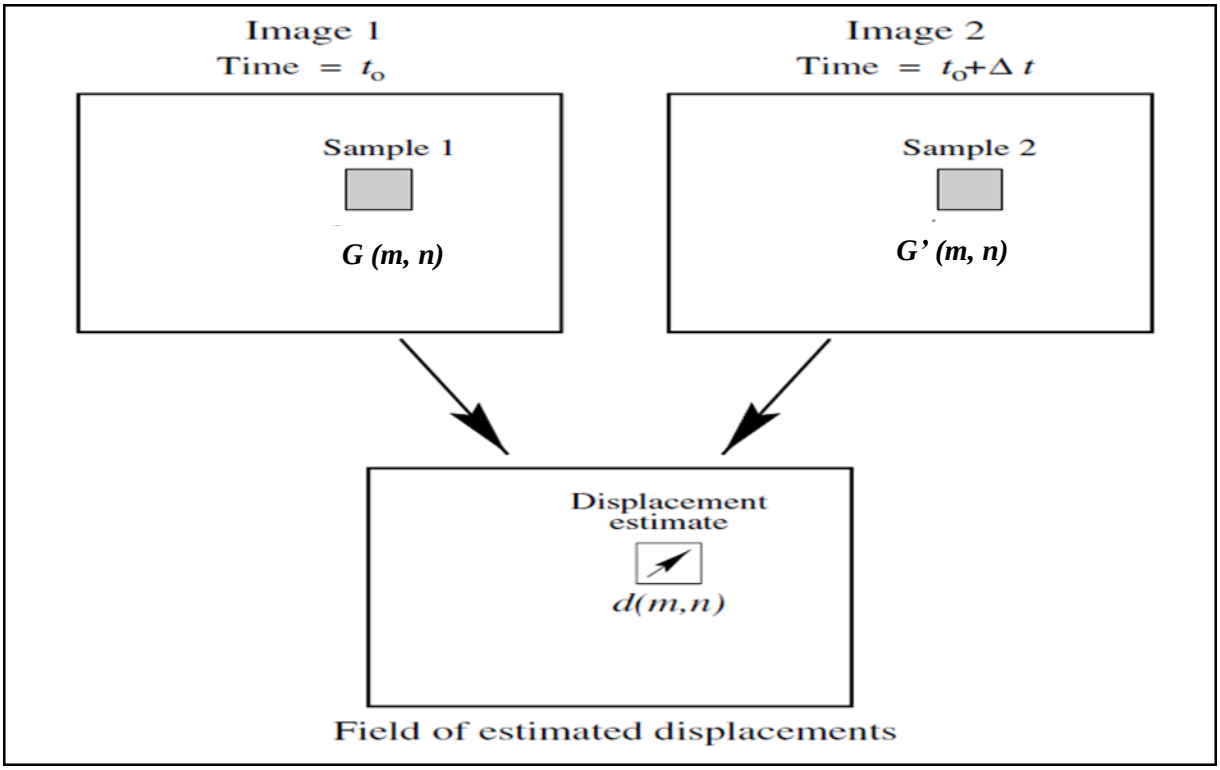

Figure 2-11 Conceptual arrangement of samples (interrogation windows) (Raffel et al., 2007)

translation of groups of particles can be observed. The image pair can yield a field of linear displacement vectors where each vector is formed by analyzing the movement of localized groups of particles. In practice, this is accomplished by extracting small samples or interrogation window and analyzing them statistically (Fig. 2-11). The method of choice is to locally find the best match between the images in a statistical sense. Usually this is done through the use of the discrete cross-correlation function.

$$R_{II}(x,y) = \frac{\sum_{i=-K}^{K}\sum_{j=-L}^{L} G(i,j)G'(i+x,j+y)}{\sqrt{\sum_{i=-K}^{K}\sum_{j=-L}^{L} G^2(i,j)}\sqrt{\sum_{i=-K}^{K}\sum_{j=-L}^{L} G'^2(i+x,j+y)}} \quad (2\text{-}6)$$

The variables G and G' are the samples (e.g. intensity values) as extracted from the images where G' is larger than the template G. Essentially the template G is linearly 'shifted' around in the sample G' without extending over edges of G'. For each choice of sample shift (x, y), the sum of the products of all overlapping pixel intensities produces one cross-correlation value $R_{II}(x, y)$. By applying this operation for a range of shifts ($-M \leq x \leq +M$, $-N \leq y \leq +N$), a correlation plane the size of $(2M+1) \times (2N+1)$ is formed. This is shown graphically in Fig. 2-12. For shift values at which the samples' particle images align with each other, the sum of the products of pixel intensities will be larger than elsewhere, resulting in a high cross-correlation value $R_{II}(x, y)$ at this position (Fig. 2-13). Essentially the cross-correlation function statistically measures the degree of match between the two samples for a given shift. The highest value in the correlation plan can then be used as direct estimate of the particle image displacement. As long as the time intervals between two successive images are already known, velocities can be calculated straightforward.

Typical PIV is designed for studying flow motions, using the motion of seeding particles that match the fluid properties reasonably well to calculate the velocity field of the fluid being studied. However, the current system focuses on measuring the velocity of sediment rather than fluid, so the sediment particles are assumed traceable particles to calculate velocities.

Because of this, one severe problem occurs in the PIV analysis. As Keane and Adrian (1992) demonstrated, PIV requires roughly ten tracer particle images per interrogation region to accurately resolve local particle displacement using traditional correlation. If the seeding density is low, particle tracking velocimetry (PTV) can be used to follow

individual particles but he seeding density itself severely limits spatial resolution as particles exist within the interrogation region. At high seeding densities, it becomes difficult to match pairs of particle images. In current study, the concentration of sediment particles is fluctuating and particle densities in the recording region are inhomogeneous. Both low seeding density and extremely high density can occur along with the changing of flow in laboratory experiments. Moreover, as the current study utilizes an EL-sheet as a light source, traceable pattern will disappear due to the large concentration, which makes the PIV analyses break down in the previous measurement system. Hence, in order to overcome the problem of velocity analysis, a stroboscope is introduced as an additional light source to illuminate the highly concentrated sediment particles. Detailed explanation of the function of the stroboscope will be introduced in the verification test.

Chapter3. Verification tests of the measurement system

In order to check the performance of the measurement system, a serious of verification tests were carried out. Firstly, similar verification tests with Masame (2013) were conducted to determine the measuring limit of the previous system. And then verification tests for the improved system were performed to validate the feasibility in measuring highly concentrated sediment flux.

3.1 Determination of the measuring limit of the existing system

As mentioned above, density of tracer particle is an important factor in the PIV system. Either high or low tracer particle density will cause troubles in velocity analysis. Masame (2013) indicated that the measurement system would break down when the sediment concentration is high, and the factor of light attenuation around 2.5 is regarded as the measuring limit of the existing system. For the sake of reifying the measuring limit, a sequence of verification tests was carried out.

3.1.1 Verification tests method

The configuration of verification tests is shown in Fig. 3-1. An EL-sheet (20×15 cm) was stuck on the backside wall of a transparent flume. The model flumes were made of acrylics with lengths of 50 cm, heights of 15 cm and different widths. On one side of the flume there was a PVC tube connected to tap water, which was used for generating flow. Silica sands with median diameter of 0.16 mm were released into model flumes through a simple sediment fall device, and the sand would move under the resultant force of the

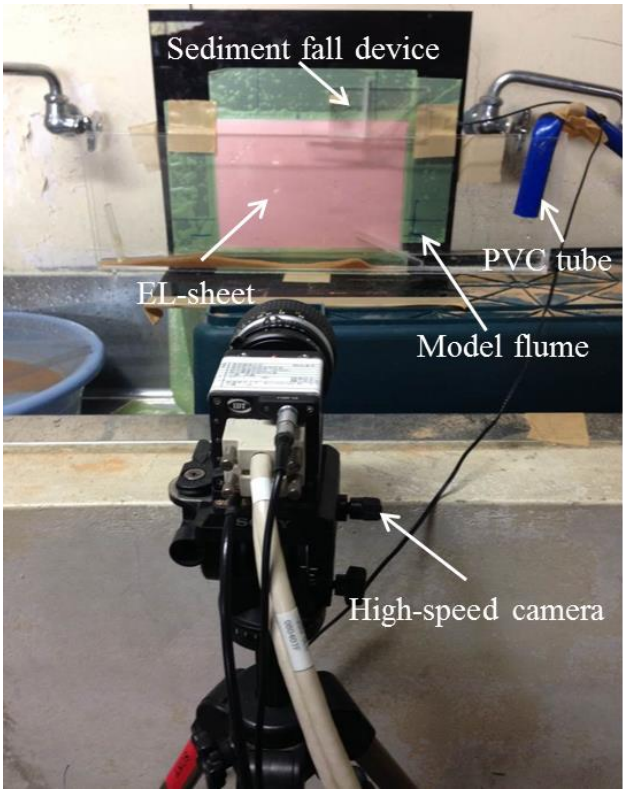

Figure 3-1 Experimental setup of verification tests for determine the

Table 3-1 Experimental conditions of verification tests for determine the

Path Length(cm)	case					
	1	1.5	3	4	5	6
1	4.48g	5.11g	5.28g	5.6g	6.38g	8.1g
1.5	7.12g	7.74g	8.33g	8.62g	10.32g	11.42g
2	4.38g	4.45g	6.1g	6.36g	6.93g	7.09g
3	6.58g	7.13g	7.45g	7.92g	9.41g	9.61g
4	8.12g	9.4g	11.36g	13.8g	14.2g	19.13g
5	11.76g	14.22g	14.3g	15.37g	15.84g	17.07g

gravity and flow. Thus, the process is similar with sediment suspension. The high-speed camera was 30 cm from the model flumes. And by using a lens with fixed 50mm focal length, the setup gives a resolution parameter λ=100 um/pixel. The camera was set in an fps of 500 to record the movement of the sands. Six model flumes with a width of 1.0

cm, 1.5 cm, 2.0 cm, 3.0 cm, 4.0 cm and 5.0 cm separately were used in the verification tests. For each model flume, six different weights of sands were released into the flow. Detailed experimental conditions of verification tests for determine the measuring limit of the previous system is listed in Table 3-1. Examples recorded images of verification tests are given in Fig. 3-2.

3.1.2 Verification tests result

For each case, several inspection lines were set to measure sediment flux and interval between two adjacent inspection lines was 40 pixels. On each inspection line, velocity was calculated in a distance interval of 12 pixels. Interrogation widow with a size of 24 $\times$24 pixels were applied in PIV analysis. Mean value of the light intensity of the interrogation window was used to calculated the concentration based on the previous concentration calibration result. Thus, the overlap between interrogation areas was 50%, giving a 47$\times$16 velocity vector grid and concentration grid with a spatial resolution between 4.7 mm and 1.6 mm. Therefore, sediment flux can be calculated in every inspection line, and calculated result can be used for check the stability and accuracy of the measurement system. Example results of velocity and concentration measurement are shown in Fig. 3-3 and Fig. 3-4. Detailed result of the verification tests for determining the measuring limit of the previous system is illuminated in Table 3-2.

Result of verification tests draws a similar conclusion with Masame (2013) as follows:

(1) Sediment flux measurement system performs well when the concentration is not very high, usually the errors can be within 10% or even smaller, while it will break down when the concentration goer high. By comparing the measured weight in different

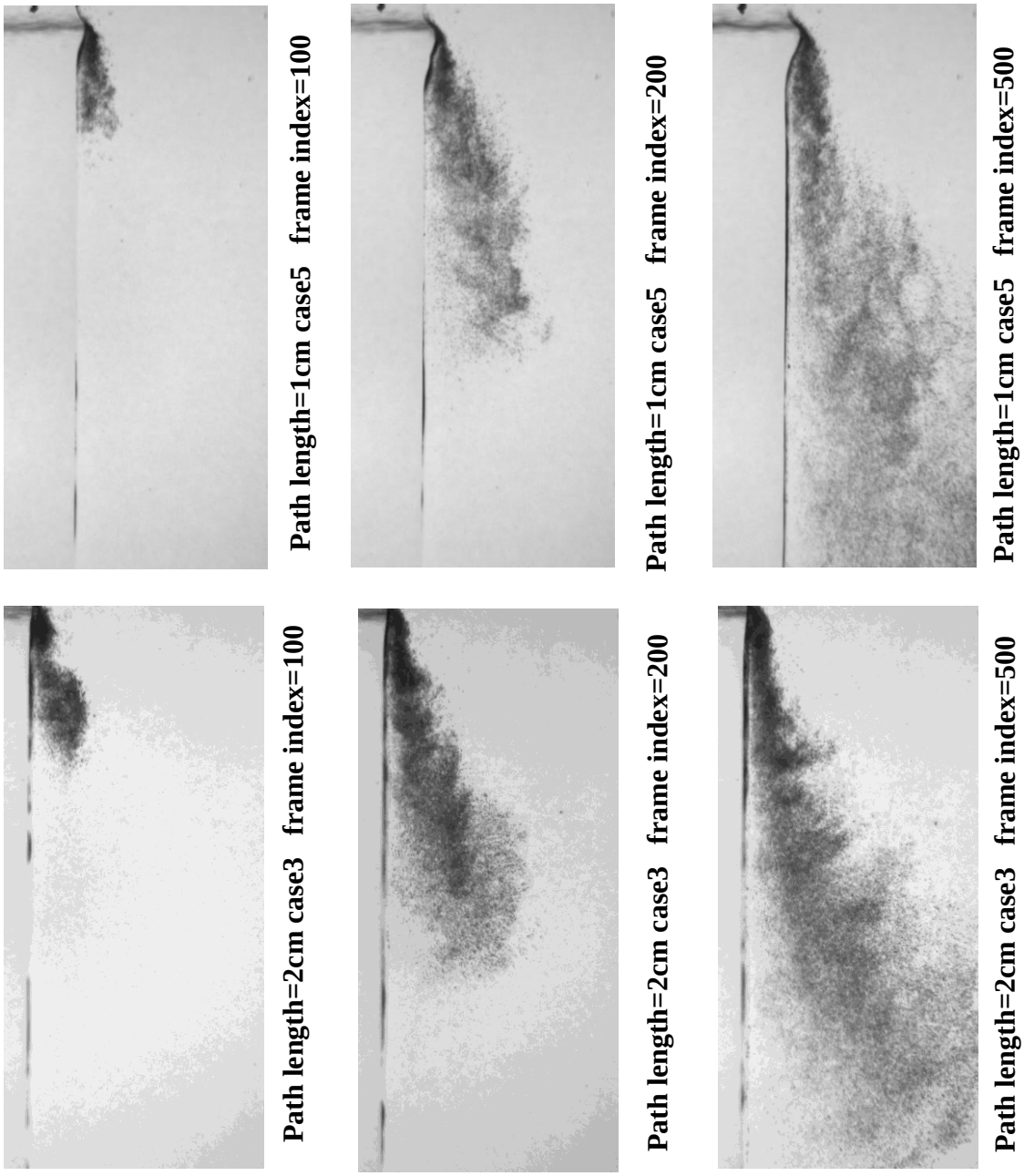

Figure 3-2(a) Examples recorded images of verification tests (images were rotated 90 degrees counterclockwise)

inspection lines, the system is considered as highly stable when concentration is not high. The main reason for failure is the breaking down of velocity analysis due to the missing of traceable pattern at that case (e.g. Fig. 3-3(b)).

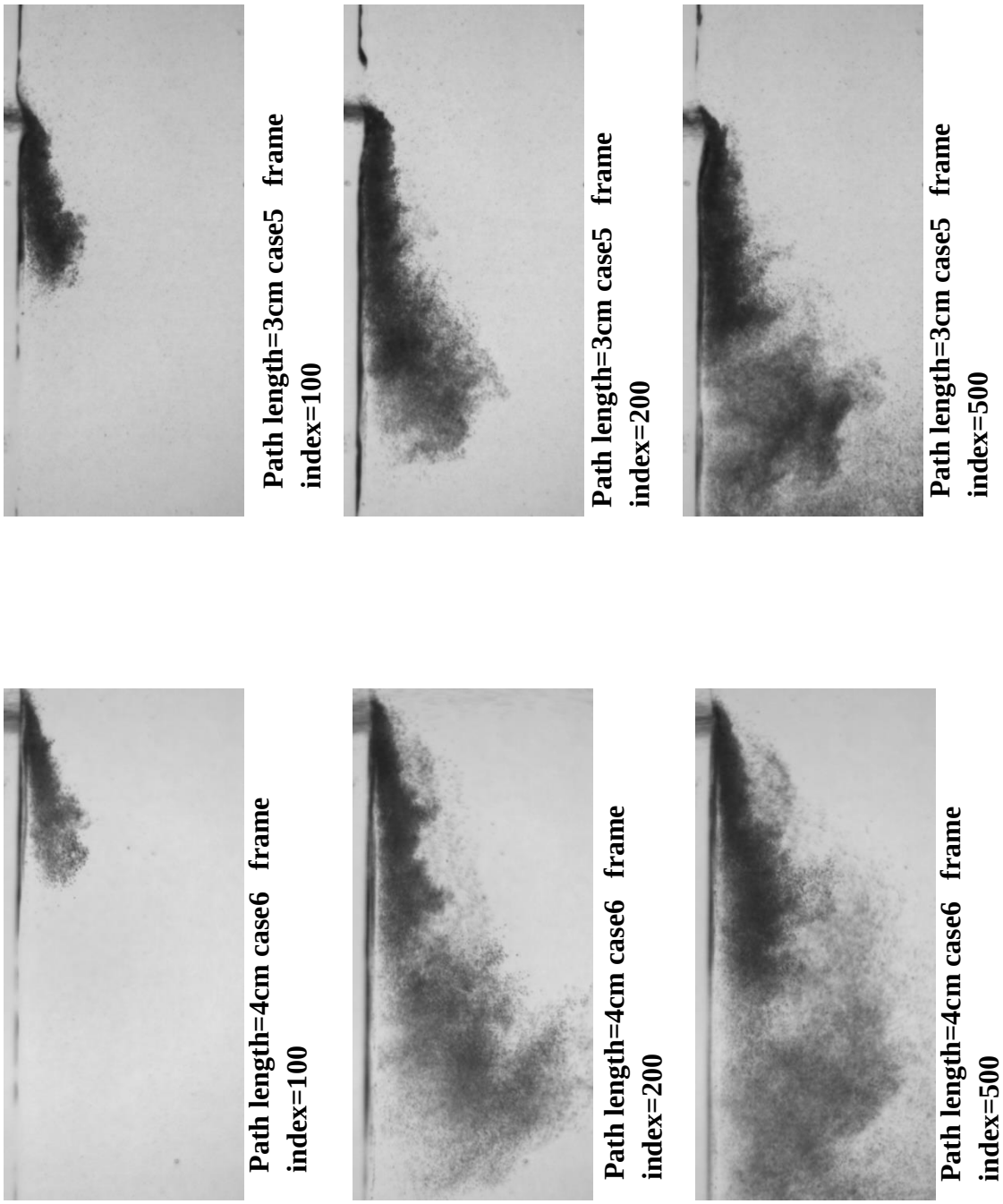

Figure 3-2(b) Examples recorded images of verification tests (images were rotated 90 degrees counterclockwise)

(2) The factor of light attenuation in 2.5 can be regarded as the measuring limit of the existing system. In most cases, PIV did well below 2.5 of the factor of light attenuation. Otherwise, the measurement system would be inaccurate because there is no reliable

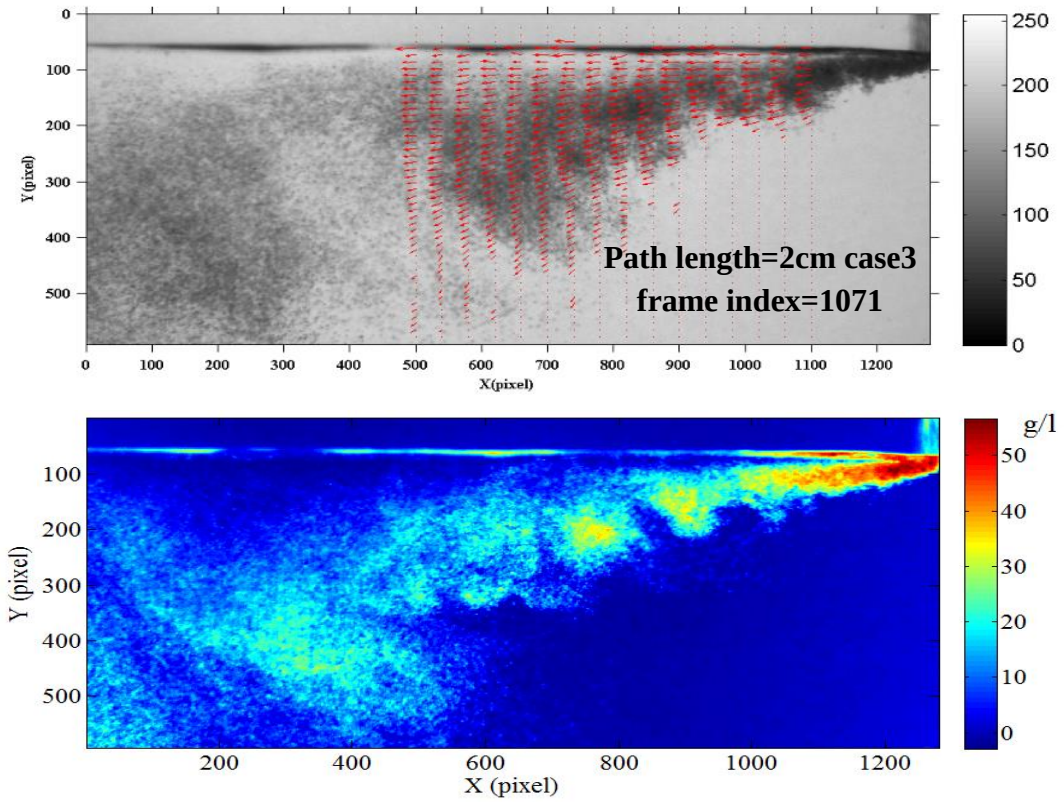

Figure 3-3(a) Example results of velocity and concentration measurement for determining the measuring limit

velocity result. When the light attenuation exceed 2.5, precise velocity result is difficult to obtain even using large interrogation window or other post-processing methods (e.g. multiple iteration cross-correlation method) for PIV.

(3) Measuring range will narrow down along with the increasing of the path length. In the section of concentration calibration, it has been indicated that the relationship between concentration and light attenuation is not always linear. The relation curve levels off after the sediment concentration reaches a critical value. This critical value will decrease along with the increasing of the path length, which lead to the decreasing of measurable range of concentration. Moreover, because of the short distance between the light source and the high-speed camera in small path lengths, traceable patterns will disappear in a higher concentration than large path lengths.

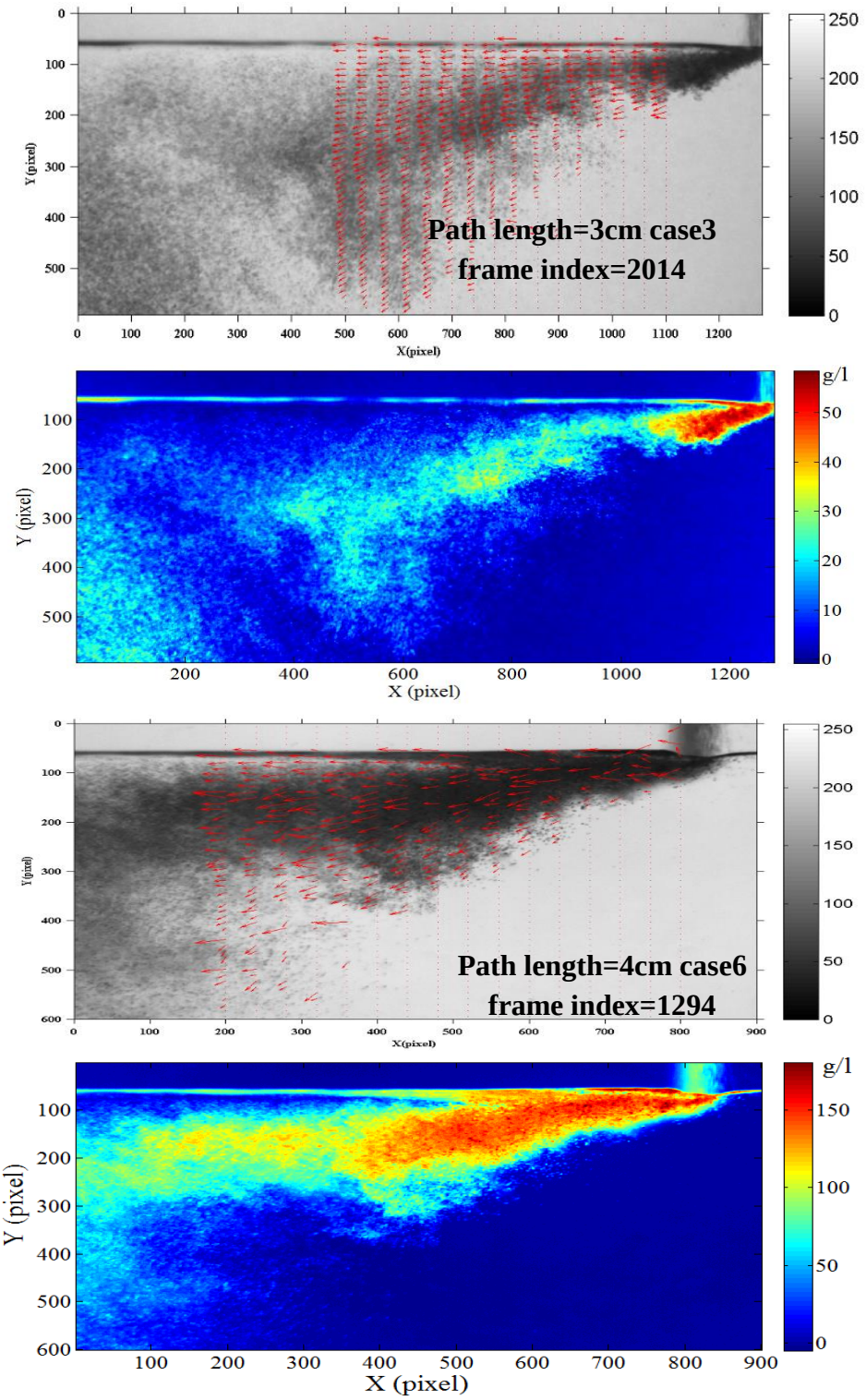

Figure 3-3(b) Example results of velocity and concentration measurement for determining the measuring limit

Table 3-2 Detailed result of the verification tests for determining the measuring limit

Path length(cm)	Input weight(g)	Inspection line									
		1		2		3		4		5	
		Measured weight	Error(%)	Measured weight	Error(%)	Measured weight	Error(%)	Measured weight	Error(%)	Measured weight	Error(%)
1	4.48	4.62	3.19	4.66	3.91	4.59	2.46	4.67	4.17	4.67	4.17
	5.11	5.35	4.76	5.36	4.97	5.21	2.02	5.28	3.32	5.32	4.10
	5.28	5.35	1.42	5.37	1.75	5.57	5.42	5.54	4.89	5.37	1.61
	5.6	5.77	3.07	5.71	2.05	5.89	5.18	5.8	3.60	5.81	3.82
	6.38	6.59	3.22	6.66	4.33	6.62	3.76	6.58	3.07	6.6	3.43
	12.1	10.03	-17.19	9.82	-18.93	9.64	-20.41	9.91	-18.18	10.12	-16.45
1.5	7.12	7.25	1.81	7.24	1.64	7.28	2.23	7.31	2.72	7.22	1.42
	7.74	7.97	2.94	7.67	-0.91	7.49	-3.25	7.68	-0.74	7.73	-0.17
	8.33	8.5	2.08	8.63	3.55	8.62	3.49	8.66	3.99	8.62	3.52
	8.62	8.43	-2.23	8.5	-1.36	8.8	2.12	8.56	0.71	8.35	-3.15
	10.32	10.71	3.78	10.78	4.47	10.68	3.53	10.8	4.68	10.75	4.14
	15.42	12.13	-21.34	12.04	-21.92	11.03	-28.47	12.44	-19.33	11.57	-24.97
2	4.38	4.64	3.00	4.66	6.49	4.66	6.49	4.74	8.21	4.56	4.18
	4.45	4.69	5.43	4.85	8.98	4.76	7.03	4.78	7.38	4.84	8.77
	6.1	6.41	5.07	6.14	0.69	6.4	4.85	6.12	0.41	6.13	0.44
	6.36	6.49	2.04	6.73	5.82	6.65	4.53	6.72	5.64	6.6	3.79
	9.93	7.41	-25.38	8.02	-19.23	7.37	-25.78	7.11	-28.40	7.6	-23.46
	12.09	9.7	-19.77	8.72	-27.87	10.17	-15.88	9.64	-20.26	10.32	-14.64
3	6.58	7.16	8.77	6.85	4.08	6.88	4.59	7.1	7.94	6.98	6.06
	7.13	6.85	-3.88	6.91	-3.05	7.75	8.71	7.35	3.10	7.02	-1.52
	7.45	7.54	1.24	7.61	2.11	7.59	1.88	7.54	1.18	7.51	0.77
	7.92	8.4	6.10	8.39	5.93	8.46	6.83	8.49	7.19	8.51	7.51
	13.41	11.81	-12.00	11.67	-13.04	10.62	-20.86	10.68	-20.42	12.52	-6.71
	19.61	16.11	-17.85	15.81	-19.38	15.93	-18.77	16.85	-14.07	15.98	-18.51
4	8.12	8.56	5.36	8.43	3.82	8.7	-0.68	8.1	-0.21	8.58	5.68
	9.4	11.2	19.15	11.19	19.05	11.66	24.01	11.72	25.03	11.75	24.97
	11.36	11.56	1.77	12.12	6.65	10.32	-9.19	10.52	-7.16	11.62	2.31
	13.8	14.02	1.59	14.9	7.99	14.65	6.16	14.15	2.53	14.62	5.94
	14.2	13.15	-4.20	15.06	6.05	14.74	3.81	15.06	6.04	14.91	5.04
	19.13	17.31	-9.51	16.4	-14.29	15.3	-20.02	15.62	-18.33	17.34	-9.36
5	11.76	14.3	21.60	15.21	29.34	13.84	17.69	13.36	13.61	14.53	23.54
	14.22	16.28	14.49	10.32	-27.43	12.03	-15.40	11.24	-20.96	12.2	-14.19
	14.3	12.35	-13.64	16.36	14.41	10.38	-27.41	10.78	-24.61	10.64	-25.63
	15.37	13.28	-13.64	16.36	14.41	10.38	-27.41	10.78	-24.61	10.64	-25.63
	15.84	13.28	-13.79	12.24	-20.36	12.58	-18.12	13.32	-13.33	13.11	-14.74
	17.07	19.23	12.65	13.54	-20.68	19.33	13.24	20.21	18.39	15.35	-10.09

(4) Sediment flux measurement system will be unstable when the path lengths are too large (e.g. path length=4.0cm). One reason is that the large path length makes the traceable patterns disappear in a low concentration. Another reason is that the flow is

significantly turbulent when large budgets of sands fall into the flume in that case, which results in the difficulties in velocity analysis.

In summary, previous sediment concentration measurement system performs well with high accuracy and stability in low concentration, while it can only measure a certain concentration range of sediment flux. Light attenuation can be used as an indicator of the measuring limit. Measuring range decreases with the increasing of the path length and large path length is regarded as inadvisable for the measurement system.

3.2 Verification tests for the improved measurement system

Application scope of the previous system is limited by the measuring range, so an improved sediment flux measurement system was developed to enlarge the measuring range. It has been described detailed in chapter 2. Main feature of the improved system is the stroboscope, which is used as an additional light source to illuminate the highly concentrated sediment flux. The application of the stroboscope is expected to overcome difficulties in velocity analysis when sediment concentration is high. Simple verification tests were carried out to study the feasibility of the improved measurement system.

3.2.1 Verification tests method

Verification tests method for the improved measurement system is similar with that conducted for determining the measuring limit for the existing system. Fig. 3-4 illuminates the side view of the verification test configuration for the improved sediment flux measurement system. In current verification test, the width of the transparent flume was 1.5 cm, which is regarded as a suitable path length for the

measurement system. Different with the former verification tests for determining the measuring limit of the previous measurement system, there was no moving flow generated by tap water. In other words, water in the tank was still, which made the test condition simpler. Silica sands in a medium diameter of 1.6 mm were released into the tank by a simple fall device, through a simple sediment fall device, which was used for falling sand uniformly in cross-flume direction. The high-speed camera was set at 400 frames per second to record the movement of the sands and the stroboscope was synchronized at a frequency of 200Hz. High quality images were obtained by high-speed camera after appropriate position adjustment of the stroboscope. As the frequency of the stroboscope is half of the camera fps, normal (back-light only) and strobo-illuminated images were alternately obtained at a same rate of 200 Hz. Normal images were used for concentration measurement and both of the two sets recorded images were employed for velocity analysis. Similar with the former verification tests, three

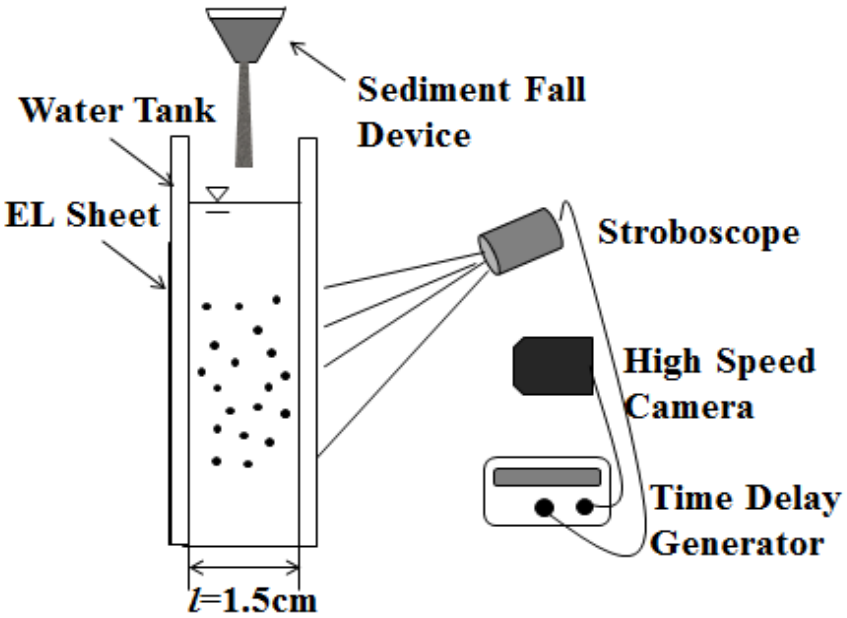

Figure 3-4 Side view of the verification tests configuration for the improved measurement system

inspection lines were set to calculate the sediment flux. As the net amount of input sand was known, the performance of the improved system could be evaluated by comparing the measured weight and actual weight. The tests were carried out for four cases of different amount of input sand.

3.2.2 Verification tests result

Examples of measured results of instantaneous velocity and concentration are presented in Fig. 3-5 and Fig. 3-6. Color bar on the right-hand side gives the concentration ranging from 0 to 200 g/l. It is obvious that velocities measured from strobo-illuminated images are better than those from normal images. Fig.3-7 shows the light intensity distributions of two adjacent images taken with and without stroboscope respectively at the same location (indicated by rectangles in Fig. 3-5). It can be confirmed that the stroboscope is capable of forming traceable patterns for operating PIV precisely by enlarging the light intensity range in the cases that sediment concentrations are very high. It should be noted that light reflection caused by the sidewall was not significant in current case and it did not influence the measurement system seriously. Thus, precise velocity analysis under the condition of highly concentrated flows was achieved.

It should be noted that concentrations around the edge area of the moving sediments is low in general, and sediment particles in this area usually disappear in the images result from the illumination of the stroboscope, such as the locations indicated by circles in Fig. 3-5. Meanwhile, velocity measurement in these areas usually fails because of the lack of pattern. In contrast, PIV performs well in the edge area of the normal images because of the low concentration. Therefore, a post processing method of velocity analysis in terms of the strobo-illuminated images was utilized to omit wrong velocity

vectors in the edge area. Since the recorded images were in gray-scale, and intensity value ranges from 0 (black) to 255 (white), a boundary value of detected light intensity was set to recognize the pattern disappearing in the edge area of the strobo-illuminated images. In current study, we found that it is appropriate to set the boundary value at 235. Once the light intensity value exceeds the boundary value, traceable patterns would

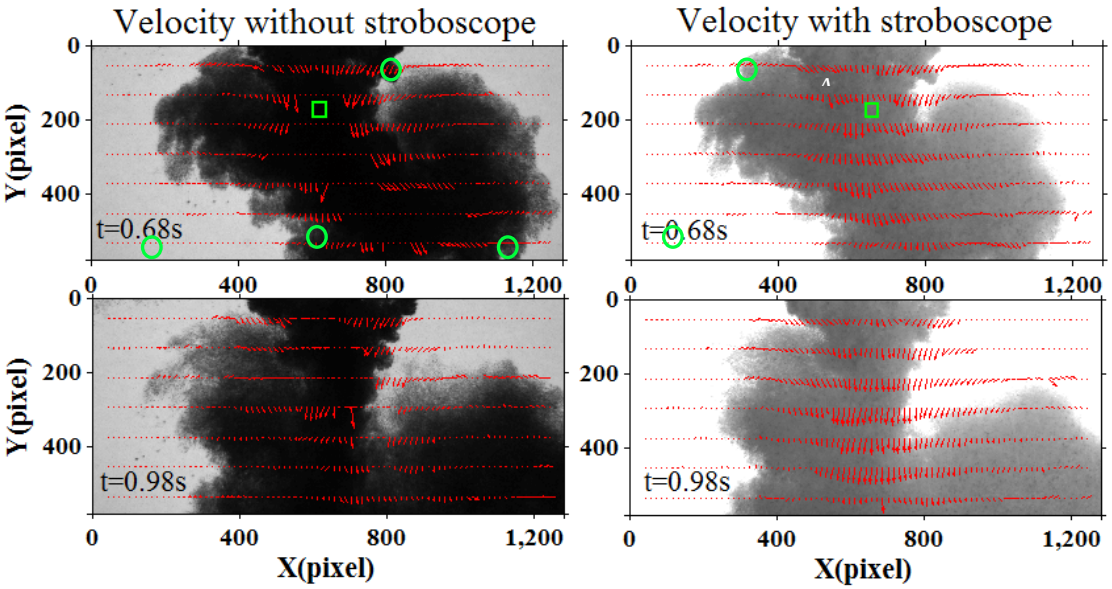

Figure 3-5 Examples of instantaneous measured velocities

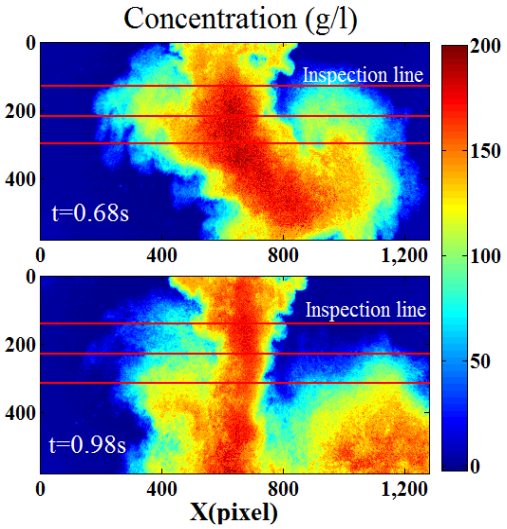

Figure 3-6 Examples of instantaneous measured concentration

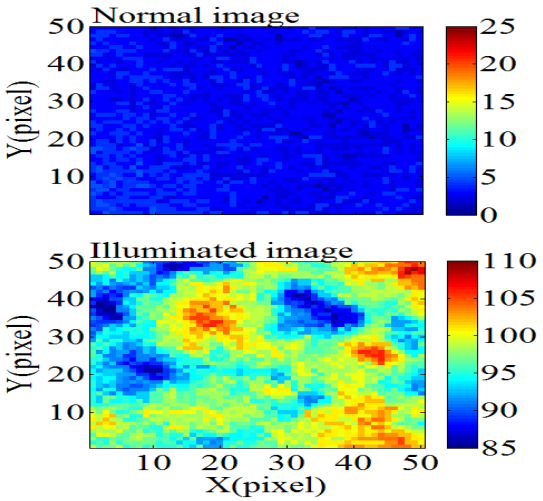

Figure 3-7 Comparison of light intensity distribution between normal image and strobo-illuminated image (real size is 0.5cm×0.5cm)

disappear in the corresponding areas and PIV analysis would break down. After recognizing the pattern disappearing areas, the velocity vectors in these areas will be replaced by those calculated from the adjacent normal image at the same locations. Thus, wrong velocity vectors are eliminated effectively.

Three inspection lines were set to measure the sediment fluxes. Since all of the input sand passed through the inspection lines, net sediment flux measured in each inspection lines should be same among each other and same with the actual input weight. The calculating formula is similar with Eq.1-1 as the following:

$$W_s = \int_0^T \int_{AA'} c u_s l dx dt \tag{3-1}$$

where *Ws* is the measured weight of sediment and *T* is the total passing time for each inspection line. c, u_s, l are concentration, velocity and path length respectively. Sediment concentration and velocity are measured at an interval of 12 pixels (about 0.1 cm in reality) along each inspection line. Both velocity results measured from normal and strobo-illuminated images were substituted into Eq. 3-1 for calculating sediment flux to check the performance of the improved system.

The results of verification tests are presented in Table 3-3. The two columns at the right of the table show the ratio of integrated fluxes to actual input amount in each inspection line. It is obvious that the measured sediment fluxes from velocities with stroboscope are much better than those from velocities without stroboscope, as all of their errors are within 10%. Moreover, those measured results from velocity results with stroboscope at each inspection line are close to each other in the same case, illustrating that

concentration and velocity measurements are consistent. Maximum and mean values of sediment concentration and light attenuation for each inspection line in every case are also presented in Table 3-3. It was found that the new system performed well beyond the measurement limit of the previous system that is light attenuation of 2.5. The maximum and mean values of light attenuation are 4.47 and 3.12 respectively. They are far more than the previous system. In this study, maximum value of measurable sediment concentration could reach as high as 193 g/l, in a path length of 1.5 cm and it is not the measuring limit of the current system.

In summary, the stroboscope is capable of illuminating the highly concentrated sediment well by careful position adjustment. Thus, the camera can capture clear particle patterns for PIV analysis and flux measurement for sediment transport of high concentrations can be achieved. The limitation of the current stroboscope is its

Table 3-3 verification tests result for the improved measurement

Case	Input weight (g)	Inspection line	Sediment Concentration (g/l)		Light attenuation		Error without strobo(%)	Error with strobo(%)
			Max	Ave.	Max	Ave.		
1	13.09	a	193.20	136.61	4.47	3.12	-34.6	-5.2
		b	184.37	135.78	4.26	3.11	-27.0	-5.6
		c	178.92	130.02	4.15	3.01	-23.1	-7.4
2	18.04	a	176.32	105.45	4.13	2.98	-41.6	-4.7
		b	175.20	103.24	4.11	2.76	-35.7	-2.4
		c	170.01	98.35	4.04	2.35	-22.2	-8.9
3	18.06	a	149.06	76.79	3.45	1.75	-13.9	-2.6
		b	149.56	73.22	3.45	1.67	-16.4	0.8
		c	145.46	70.53	3.36	1.60	-15.8	-4.0
4	19.32	a	179.68	111.33	4.47	2.69	-37.1	-7.8
		b	177.27	105.76	4.23	2.56	-26.6	-5.5
		c	171.11	101.08	4.15	2.45	-20.8	-5.2

maximum frequency. As PIV requires a short time interval between two consecutive images, the current stroboscope cannot fulfill the requirement well when the target flow is fast.

Combined illumination is essential in the measurement of sediment flux with a wide range of sediment concentration. Liu and Sato (2005) have already confirmed that only using stroboscope cannot measure the sediment concentration. On the other hand, only using brighter lens or stronger backlight sources will result in missing of small concentration band.

The improved system turned out to be successful in measuring sediment transport of high concentration. It is proved that highly concentrated sediment denser than 190 g/l in the path length of 1.5 cm could be measured accurately. Limitation in the factor of light attenuation has been broken through in the improved system. This system is expected to be used for future laboratory investigations of sediment dynamics close to the bed.

Charpter4. Laboratory study of sediment transport in the swash zone under dam-break waves

4.1 Introduction

The importance of the swash zone is widely recognized especially in the presence of a movable bottom, as with natural beaches, because a consistent part of the sediment transport takes place in it. It is well known that the intense fluid/sediment interaction that occurs in the near shore region results in sediment suspension and transport that change the coastal morphology. In this regard, the swash zone plays a very important role because it is the region of shoreline erosion and accretion. The main physical processes in the swash zone consist of flow with different frequencies induced by waves, turbulence due to wave breaking and swash-swash interaction, boundary layer flow and shear stress, long shore current; interactions with sediments and pore water; and infiltration-exfiltration (Longo et al., 2002). Hydrodynamics of the swash zone, which govern sediment transport mechanisms during wave run-up and run-down, and in large part controls beach face morphology, are determined by the above numerous physical processes.

Numerous scientists and engineers have been devoting themselves on sediment transport and hydrodynamics in the swash zone during the last several decades. However, the swash zone remains a mysterious region for us and complex problems in the swash zone make it a still-evolving science. Since the improved sediment flux measurement system is regarded as promising in investigating sediment dynamics close

to bed, laboratory experiments for study sediment transport in the swash zone under dam-break waves were carried out.

4.2 Methodology

4.2.1 Experimental setup and instrumentation

The experiments were carried out in an open channel flume at Tokyo University of Marine Science and Technology. It consists of a water reservoir built into one end of a 7.1 m long, 0.3 m wide and 0.7 high, glass-sided flume. The reservoir is fronted by a gate which can be raised to produce a large plunging wave leading to a bore which propagates towards an impermeable slope located downstream. The dimensions of the reservoir are shown in Fig. 4-1. The reservoir exit is streamlined to ensure a smooth transition for the flow from reservoir to the flume. A 1/6 transparent sloping bottom made of acrylics with a thickness of 8 mm was constructed at the other end of the flume. The slope was mounted to the side-wall of the flume to increase its rigidity. Above the slope, there was a movable bed with a thickness of 3 cm, and the sediment used were silica sands in a medium diameter of 0.16 mm.

Two laser distance sensors were employed to measure the change of the bed form before and after bore waves. The horizontal sensor is fixed above the flume to measure the position of the vertical sensor. The vertical sensor was fixed on a trolley which can slide on the track of the flume. Following the moving of the trolley, the vertical laser distance sensor can measure the distance between the laser head and the sand bed. Thus, the bed form can be determined through two laser distance sensor. A 20×15 cm EL-sheet was set upon the slope in 30 cm from the bottom of the slope. It was stuck on a 4

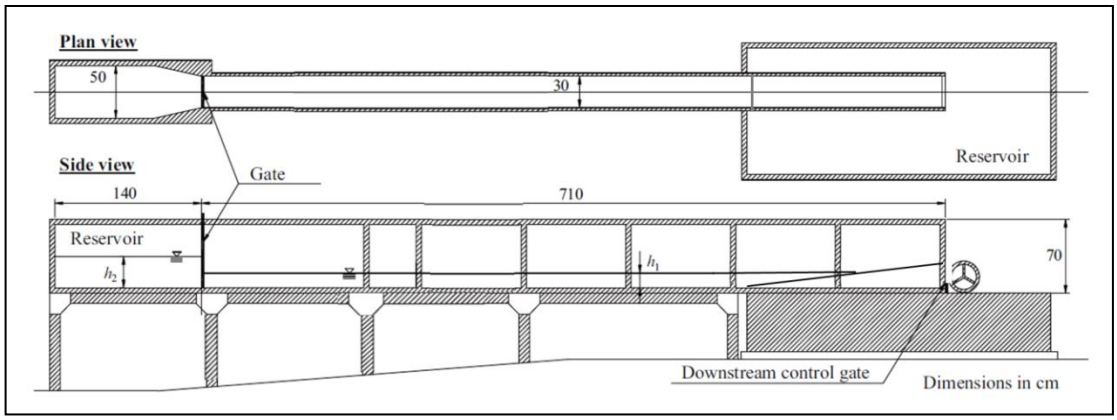

Figure 4-1 Schematic of the open channel flume

mm acrylic board, and the board was glued to the acrylic slope in perpendicular. The bottom part of the EL-sheet was under the moveable sand bed, so that sediment transport close to the bed can be observed. Distance between the EL-sheet and the side wall of the flume was 15 mm, which means the path length in current setting is 15 mm. A CMOS high-speed camera was set to record the movement of the sediments. It was rotated to be aligned with the 1/6 slope, so that the bed-normal and the bed-parallel velocities can be measured. A Nikon PK-11A Auto Extension Ring was mounted between the high-speed camera and the lens which has a fixed 50 mm focal length. The ring enabled the lens to focus closer than its normal set minimum focusing distance. And the camera was 30 cm from the target flow field which gives a resolution parameter λ=66 μm/pixel. The size of the recorded images was 520 × 1000 pixels, corresponding to a roughly 3.47 cm-by- 6.67 captured areas. The camera was controlled by specified software named Motion Studio developed by IDT Corporation. As mentioned above, PIV requires a short time interval between two consecutive images. Under bore driven swash zone, the flow is significantly turbulent, so the stroboscope used in the verification test cannot fulfill the requirement. Therefore, a new stroboscope was applied in current laboratory study. It was a double lamp stroboscope (SA-100B-W)

designed by Nissin Electronic Corporation. Each lamp has a maximum flash frequency of 120 Hz, while the time interval between the flash of two lamps can be controlled by externally triggering. After appropriate position adjustment of the two lamps, illumination effect between them can be very similar, which ensures velocity analysis will not be influenced by the different illumination effect of the two lamps. A Stanford DG645 digital delay generator was used in the experiment to accurately trigger and synchronize, which is the same one with that employed in the verification test. Schematic of the experimental setup is illuminated in Fig. 4-2.

In current study, the rate of the high-speed camera was set in1000 frames per second, and the frequency of the two lamps was 100 Hz. Time interval between two lamps was controlled in 1 μs. Thus, every 10 frames, there were 2 successive images illuminated by the stroboscope.

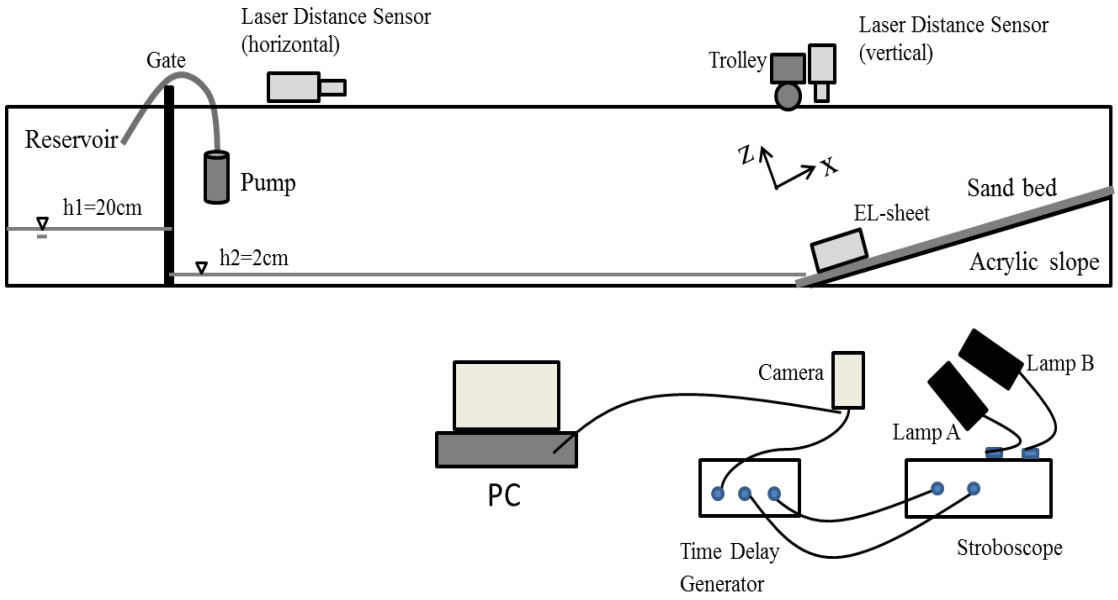

Figure 4-2 Schematic of the experimental setup

4.2.2 Experimental condition and procedure

The experiments were conducted for one initial condition only: a water depth in the reservoir of 200 mm and a water depth in front of the gate of 20 mm. The origin of the *x*-*z* coordinate system is at the initial shoreline position, located 3.2 m from the reservoir gate: the *x*-axis is parallel to the slope and is positive shoreward; the *z*-axis is perpendicular to the slope. The corresponding velocity components are *u* and *w* respectively. Measurements were triggered at the moment the wave reaches the toe of the slope, which is defined as t=0. After installing all of the instruments appropriately, experiments were conducted as the following procedures：

(1) The gate was closed and the water aspirator began to pump water from the flume to the reservoir. Because the sealing between the gate and the reservoir was not good enough, there was water leaking to the flume from reservoir. While keeping the water aspirator open, water leaking from the reservoir and pumping back to the reservoir would reach equilibrium. Since the total amount of water was carefully calculated before the experiments, the water depth in the reservoir and flume would be 200 mm and 20 mm respectively at last.

(2) Keeping the pump open, horizontal and vertical laser distance started to work for determining the initial bed from before the bore waves.

(3) The pump and gate were raised at the same time with a high speed by hand to generate dam-break wave. Simultaneously, the camera and stroboscope were triggered to work. Two lamps would flash at 100 Hz with a time interval of 0.001 s between them.

Because the bore waves will propagate about 3 seconds before reaching the slope, the camera was set to record images 3 s after getting the triggering signal.

(4) After the waves rushing down from the sand bed to the reservoir, a temporary baffle wall was lowed into the flume to compartmentalize the flume for preventing the sand bed scouring by the following seiche.

(5) Camera and stroboscope stopped to work and motion images would be saved to the hard disk.

These five steps were repeated for 20 times in order to investigate the bed form variation after multiple dam-break waves. The change of the bed form was increasingly significant with the increase of the dam-break wave number. Example images recorded by the high-speed camera were shown in Fig. 4-3.

4.2.3 Velocity analysis

Velocity analysis closing to the bottom in the swash zone is widely considered as a difficult task even without sediments. Main difficulties in velocity analysis in current study are as below,

(1) Dam-break waves are extremely turbulent, unsteady and highly non-uniform. Numerous air bubbles are generated after the break of the waves, which brings troubles to the velocity analysis when the air bubbles appear in the PIV images.

(2) Inhomogeneous suspended sediment particles make the velocity analysis distinguished from the standard PIV. It is difficult to choose an appropriate size of the interrogation widow as the concentrations of suspended sediments vary greatly. Large

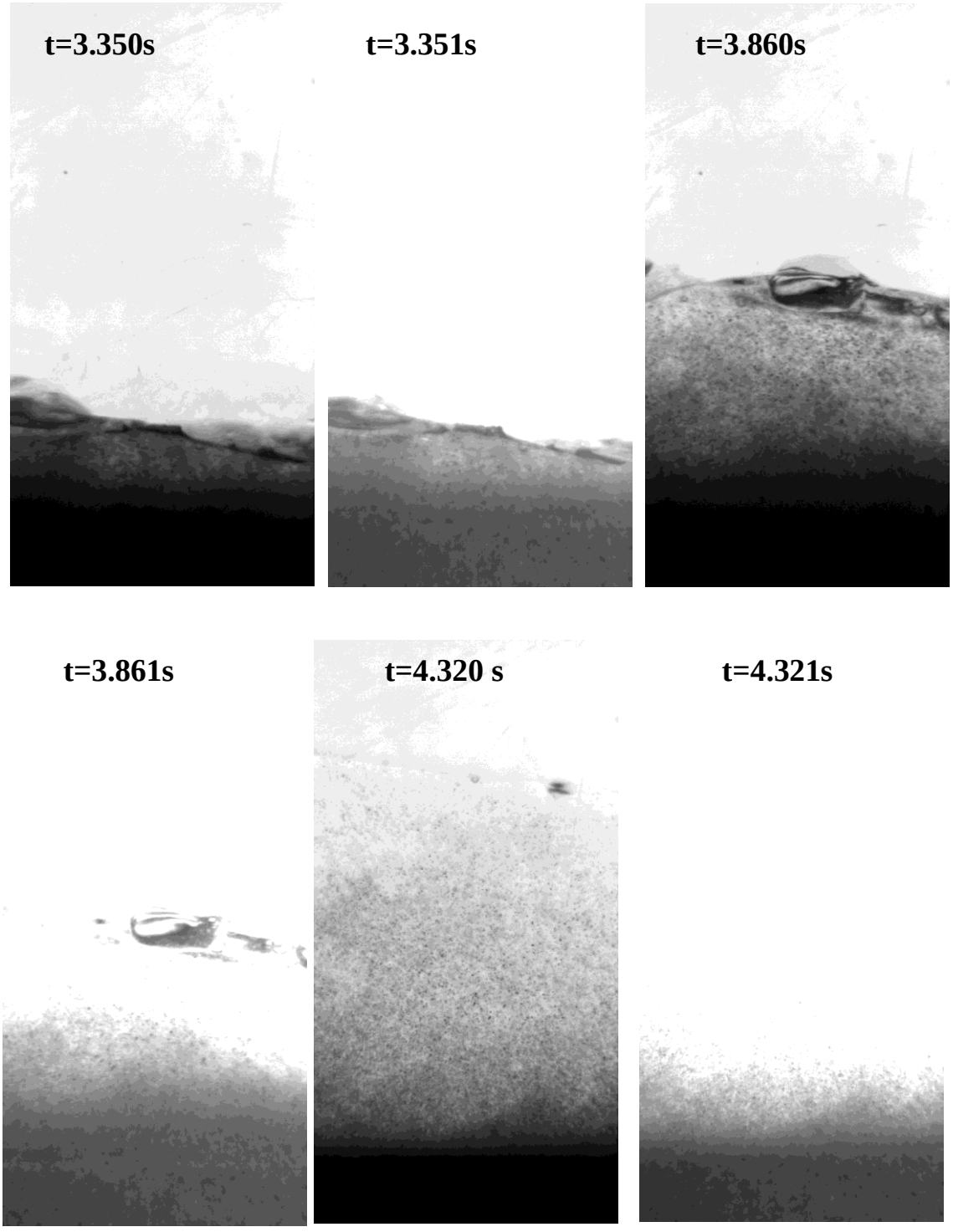

Figure 4-3(a) Example images recorded by the high-speed camera

interrogation widow is necessary when calculating velocities near the free surface as the sediment concentration is low, while this will sacrifice the spatial resolution. And

moderate interrogation widows are suitable for the middle layer of the flow. Moreover, concentrations of suspended particles are always fluctuation over time.

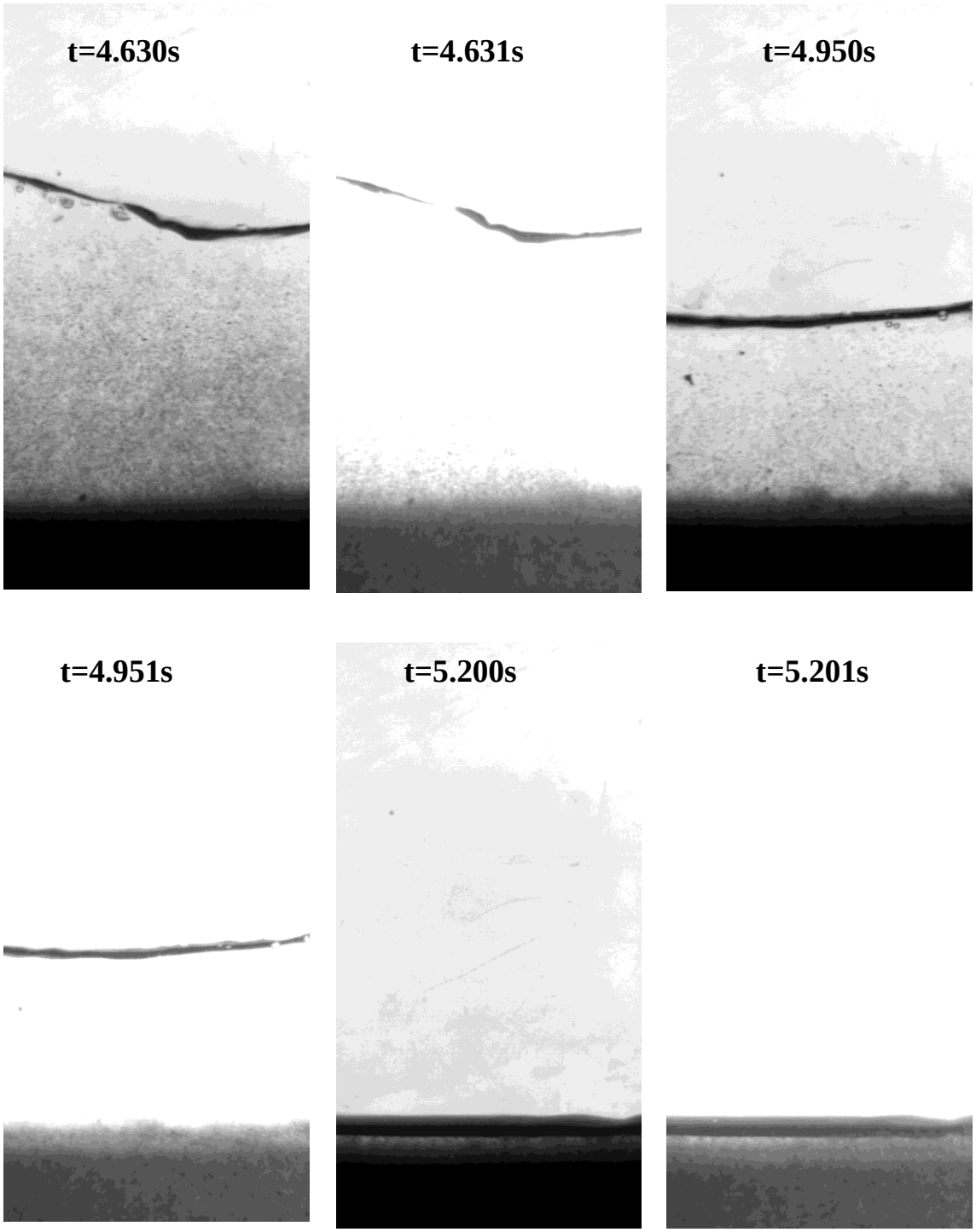

Figure 4-3(b) Example images recorded by the high-speed camera

Temporal and spatial uncertainty of the concentration of suspended sediments makes the velocity analysis difficult.

(3) Boundary between the unmovable bed and bed-load transporting sediment is hard to distinguish. So it is difficult to determine the lowest point to calculate velocity. If the lowest location is too close to the unmovable bed, than the interrogation widow will cover part of the unmovable bed, which is obviously unreasonable and results in wrong velocity vectors. On the other hand, velocity profile near the bottom will be incomplete if the lowest location is far away from the unmovable bed. Furthermore, the constantly changing bed form aggrandizes the difficulties in velocity analysis near the bottom.

In order to achieve high quality velocity results, a MATLAB-based velocity evaluation program was applied for calculating the velocity field. The algorithm used a multiple pass cross-correlation approach. A normalized local median validation operation was used to detect spurious velocity data. A parabolic peak fit was used for determination of the particle image displacement with sub-pixel accuracy. And a piecewise cubic hermit interpolating polynomial (PCHIP) method was applied for compensating the spurious data. Velocity profile with high spatial resolution and accuracy can be obtained finally. Detailed calculating processes are as follows:

(1) PIV images were cropped to cut out the useless region for decreasing the computing load. Several inspection lines in a same distance interval of 40 pixels were established vertically in the PIV images. Along each inspection line, interrogation points with a distance interval of 24 pixels were determined to perform standard cross-correlation analysis to calculate the displacement in the unit of integer pixel. Interrogation windows

in this step were chosen in 48×48 pixels, so the overlap between interrogation areas was 50%, giving a displacement grid of about 11 × 34 with a spatial resolution of 2.67 and 1.6 mm in the direction of parallel and normal to the sand bed respectively. Displacement outlier vectors were substituted by a medium value of the displacement vectors in the same row after simple outlier detection (Fig. 4-4).

(2) Second iteration of cross-correlation analysis was carried out. For this iteration, interrogation points were established in a distance interval of 16 pixels along the same inspection lines in step 1. Interrogation windows were chosen in 48 × 32 pixels, so the overlap in this step was 50% too. Displacement data in the former iteration would be used in this step to narrow the search area. For each interrogation point, the search would start from the location where the highest correlation value appears of the nearest interrogation point in the first iteration. Thus, the speed of this iteration would be significantly increased as unnecessary correlation calculations are skipped. Displacement vector grid was about 11 × 51 with a spatial resolution of 2.67 and 1.07 mm in the direction of parallel and normal to the sand bed respectively. Then displacement outlier vectors were detected and same substitution was made for these outliers (Fig. 4-5).

(5) Third iteration of cross-correlation analysis was carried out. For this iteration, interrogation points were established in a distance interval of 8 pixels along the same inspection lines in step 1 and step 2. Interrogation windows were chosen in 48 × 16 pixels, so the overlap in this step was 50% too. The displacement data in the former step were also used for offset the search area. Displacement vector grid in this step was about 11 × 104 with a spatial resolution of 2.67 and 0.53 mm in the direction of parallel

and normal to the sand bed respectively. Outlier detection was also carried out for the wrong displacement vectors.

(5) Correlation peak was estimated on the basis of the parabolic peak fit method to improve the accuracy to the order of 0.1 pixels. The equation is as follows:

$$x_0 = i + \frac{R_{(i-1,j)} - R_{(i+1,j)}}{2R_{(i-1,j)} - 4R_{(i,j)} + 2R_{(i+1,j)}} \quad (4\text{-}1)$$

$$y_0 = j + \frac{R_{(i,j-1)} - R_{(i+1,j)}}{2R_{(i,j-1)} - 4R_{(i,j)} + 2R_{(i,j+1)}} \quad (4\text{-}2)$$

Where, x_0 and y_0 are the coordinates of the correlation peak location determined by the parabolic peak fit method. i and j are the peak coordinates determined in step 4, which is in the order of integer pixel and $R_{(i,j)}$ is the maximum correlation value (Fig. 4-6).

(6) Velocity substitution between the illuminated images and normal images was carried out. In the illuminated images, image patterns disappeared where the concentrations were low. For these locations, velocities were substituted by the corresponding values of the nearest normal image. In the normal images, locations where light attenuations were larger than 2.5, velocities were replaced by the corresponding values of the nearest illuminated image (Fig. 4-7).

(7) A universal outlier detection method (Westerweel and Scarano, 2005) adapted from the original median test for the diction of spurious PIV data was performed to validate the displacement result after the former 6 steps. The advantage of this method is that it

is possible to use a single detection threshold that would be applicable for a variety of flow conditions without any prior knowledge of the flow characteristics. It is suitable for current experiments as the flow was significantly unsteady and unpredictable. The threshold value was chosen in 2 as suggested by the author. These spurious vectors were substituted by the median value in the same row (Fig. 4-8).

(8) PCHIP interpolation method was used to do interpolation for the locations where velocities vectors missed (Fig. 4-9).

(9) Outlier detection method same with step 7 was applied again after the interpolation (Fig. 4-10).

4.2.4 Concentration analysis

Sediment concentration was estimated from the previous calibration result. Sediment concentration can be visualized by translate the light intensity of every pixel. Example images of measured concentration at different moments are presented in Fig. 4-11. While it should be noted that each pixel is 1/225 mm^2 only and one sand particle occupies several pixels. Just using light intensity value of each pixel to calculate the concentration or sediment flux will bring large error. Therefore, when calculating sediment flux, concentrations were measured at the same locations where transport velocities were measured. And the mean values of light intensity of local interrogation widows centering in the interrogation point for velocity measurement were applied for measuring concentration by substituting to the previous calibration curve. Thus, sediment concentration distribution in each image has the same spatial resolution with the distribution of transport velocity.

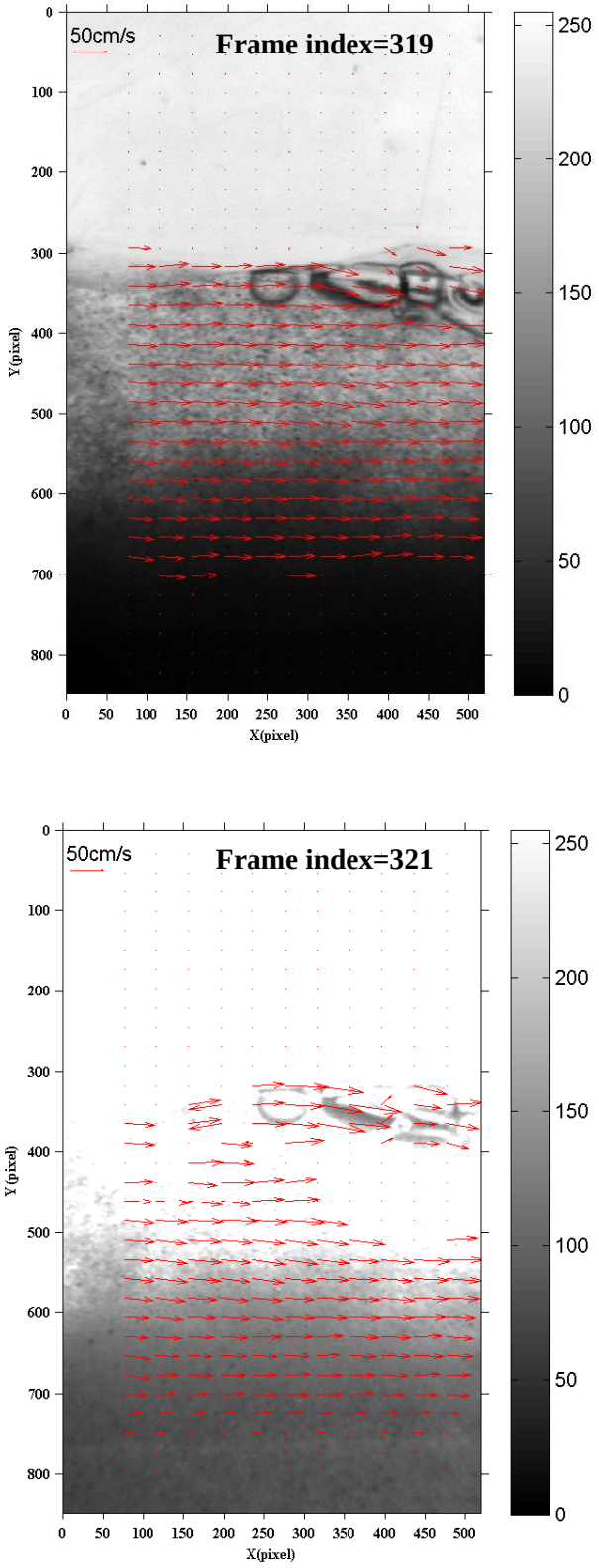

Figure 4-4 Velocity result by first iteration of cross-correlation analysis

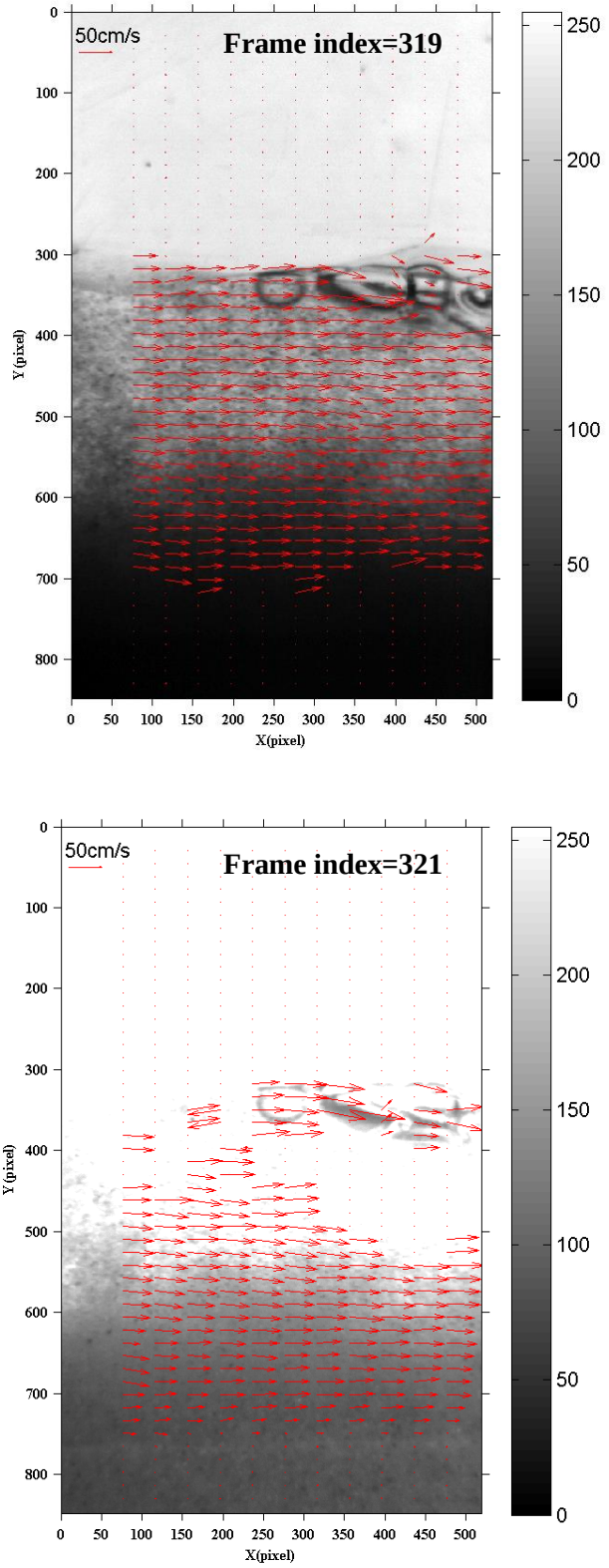

Figure 4-5 Velocity result by second iteration of cross-correlation analysis

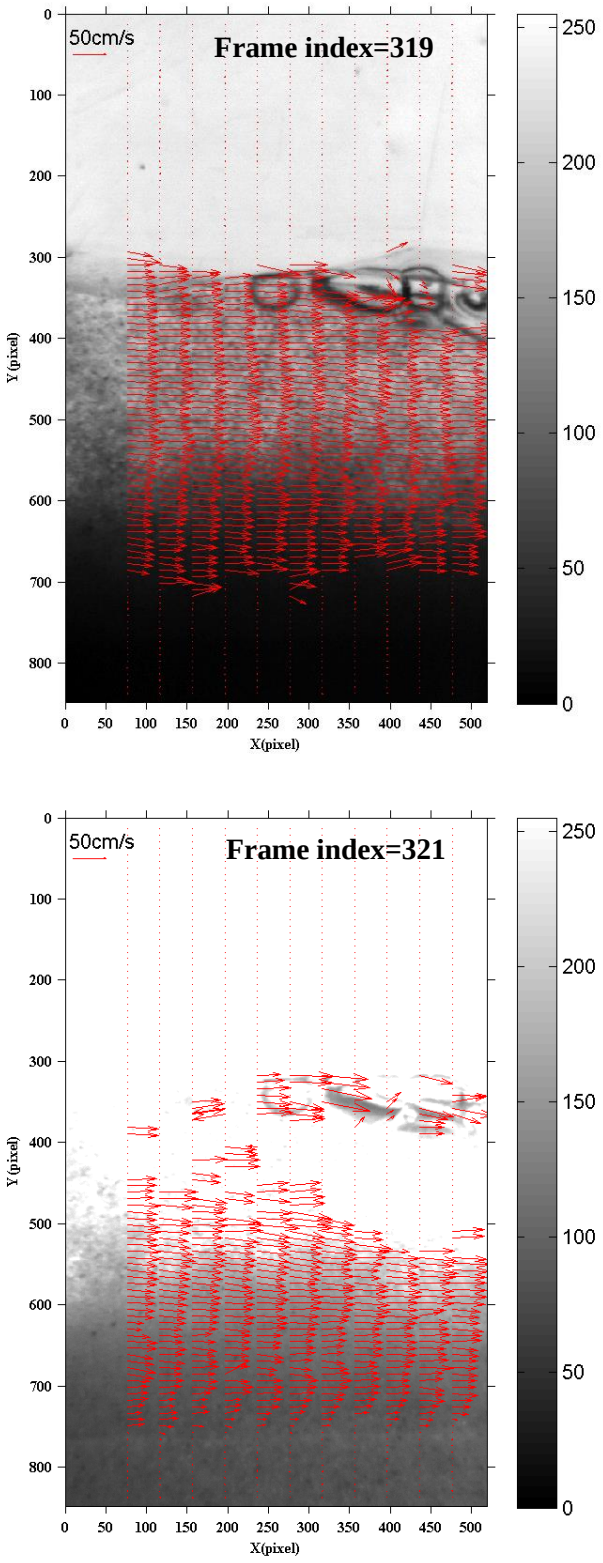

Figure 4-6 Velocity result by third iteration of cross-correlation analysis and peak detection

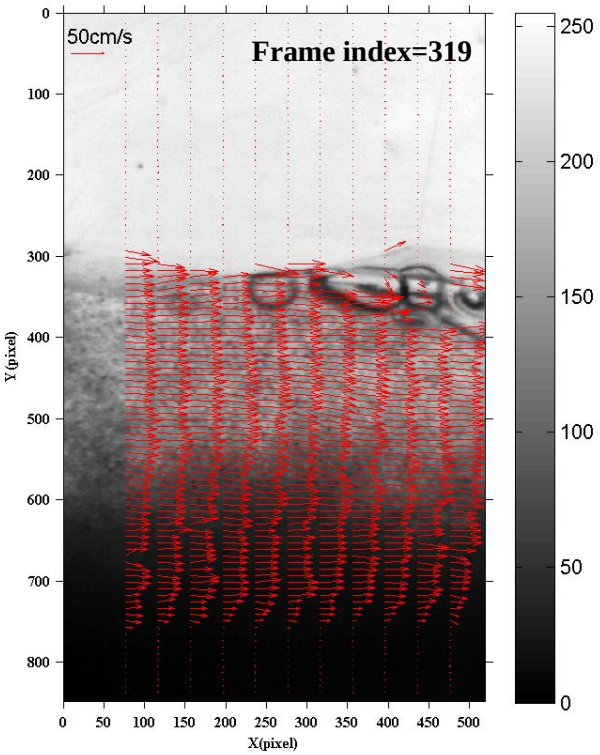

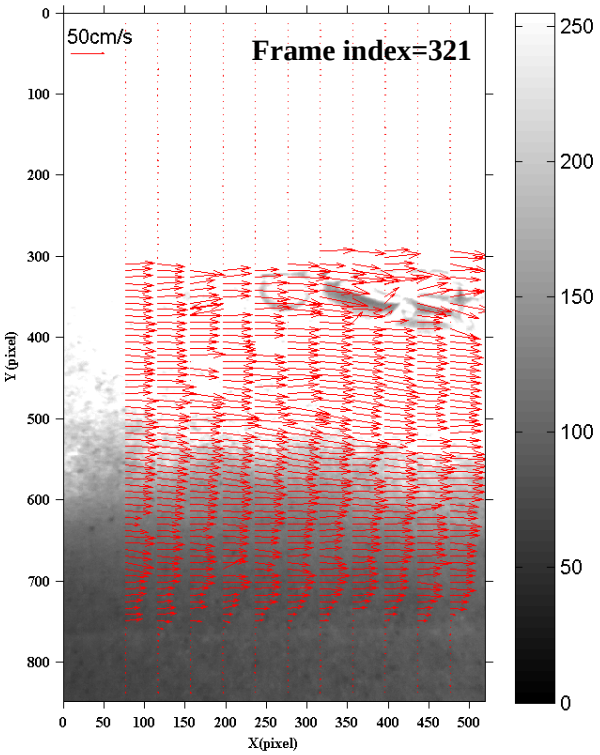

Figure 4-7 Velocity result after substitution

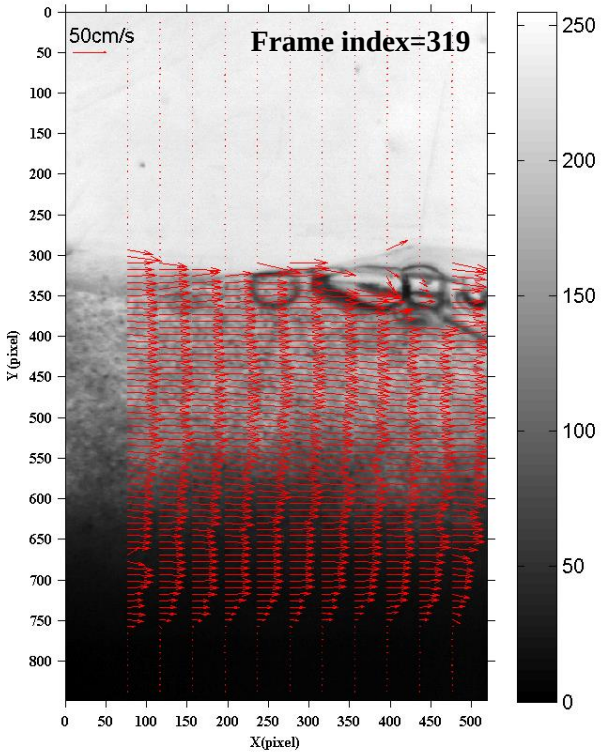

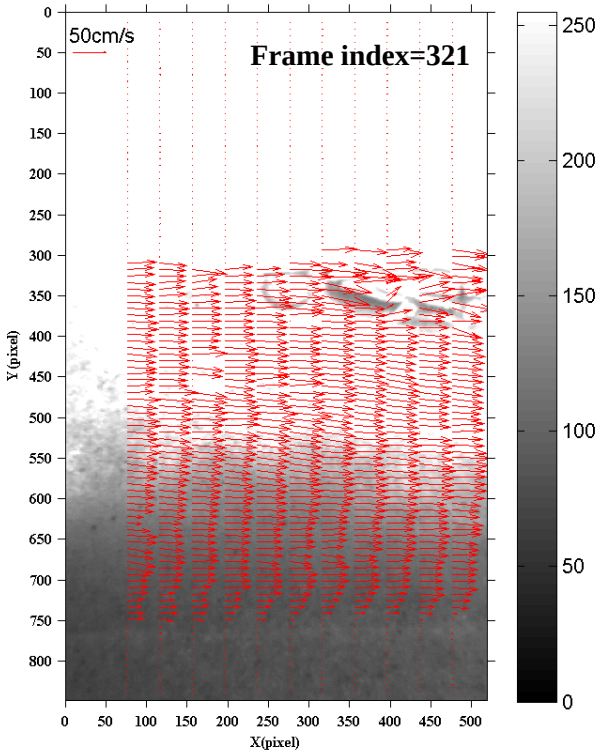

Figure 4-8 Velocity result after first outlier detection

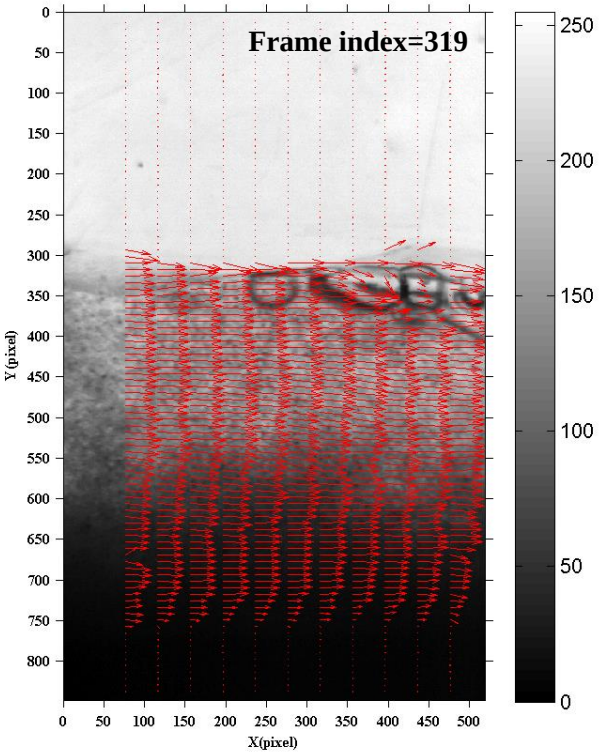

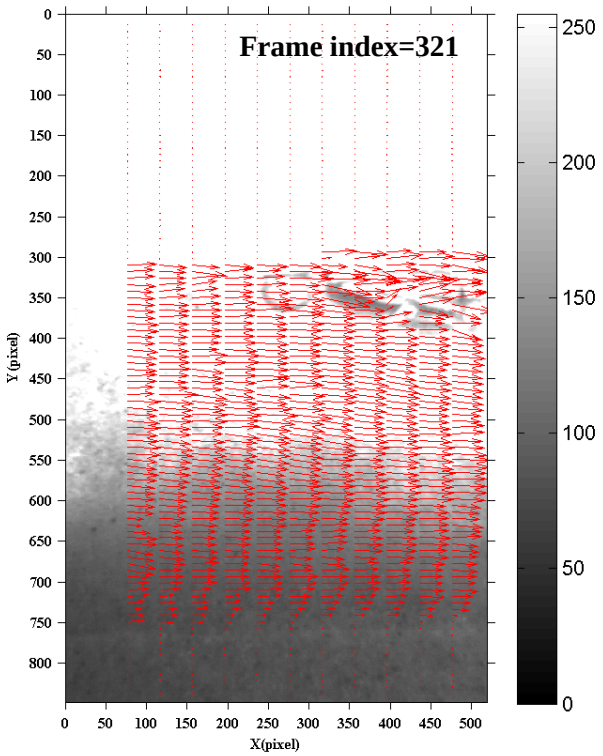

Figure 4-9 Velocity result after interpolation

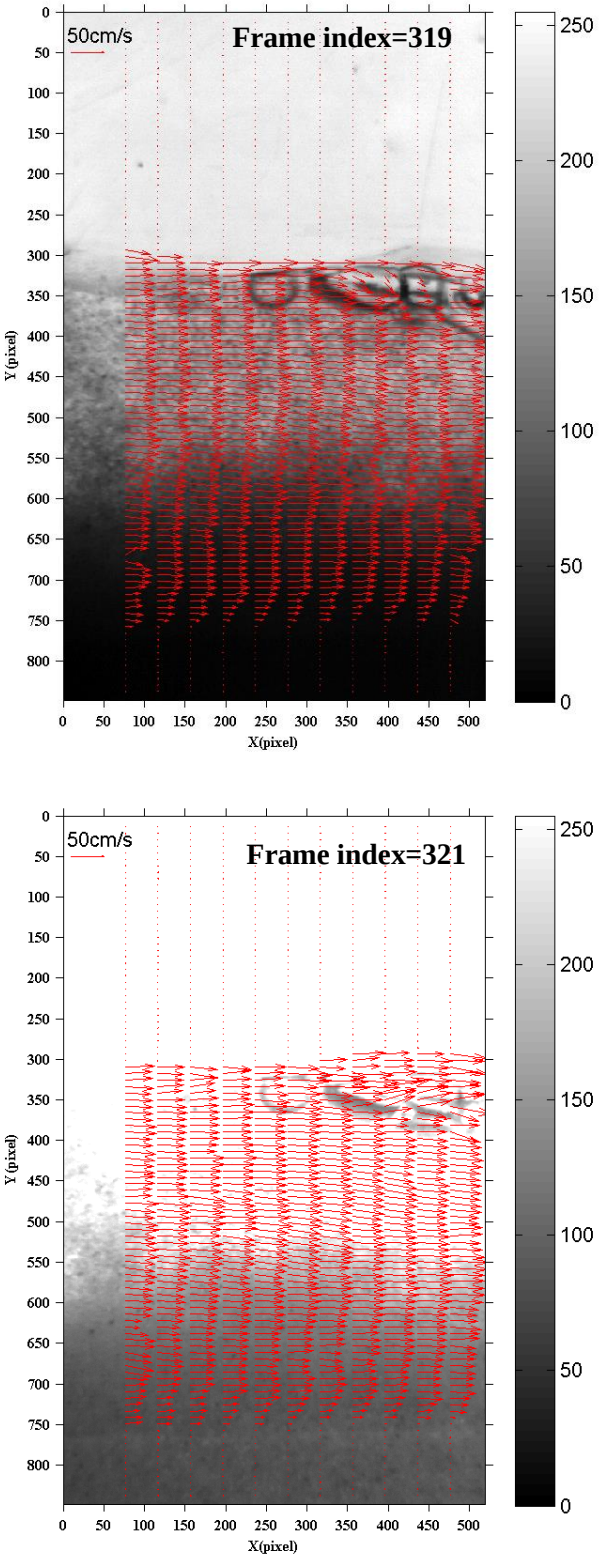

Figure 4-10 Velocity result after second outlier detection

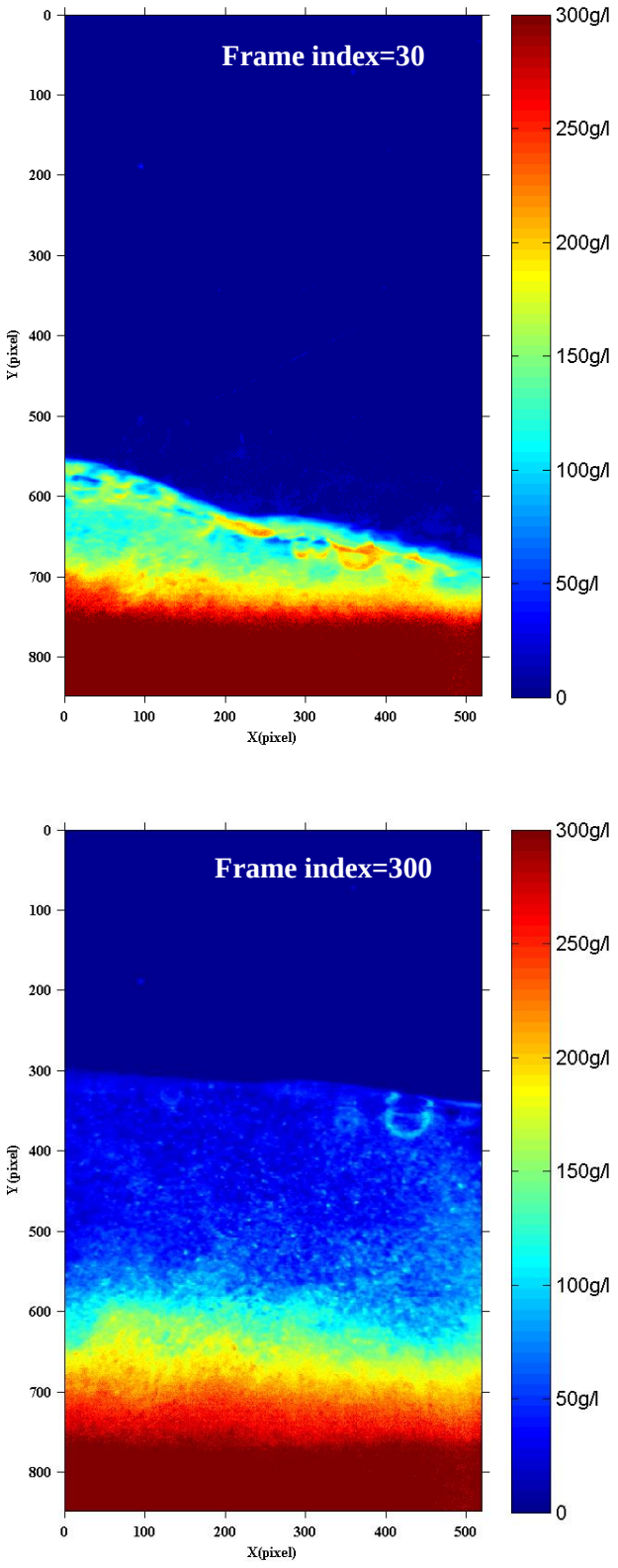

Figure 4-11(1) Example images of concentration distribution

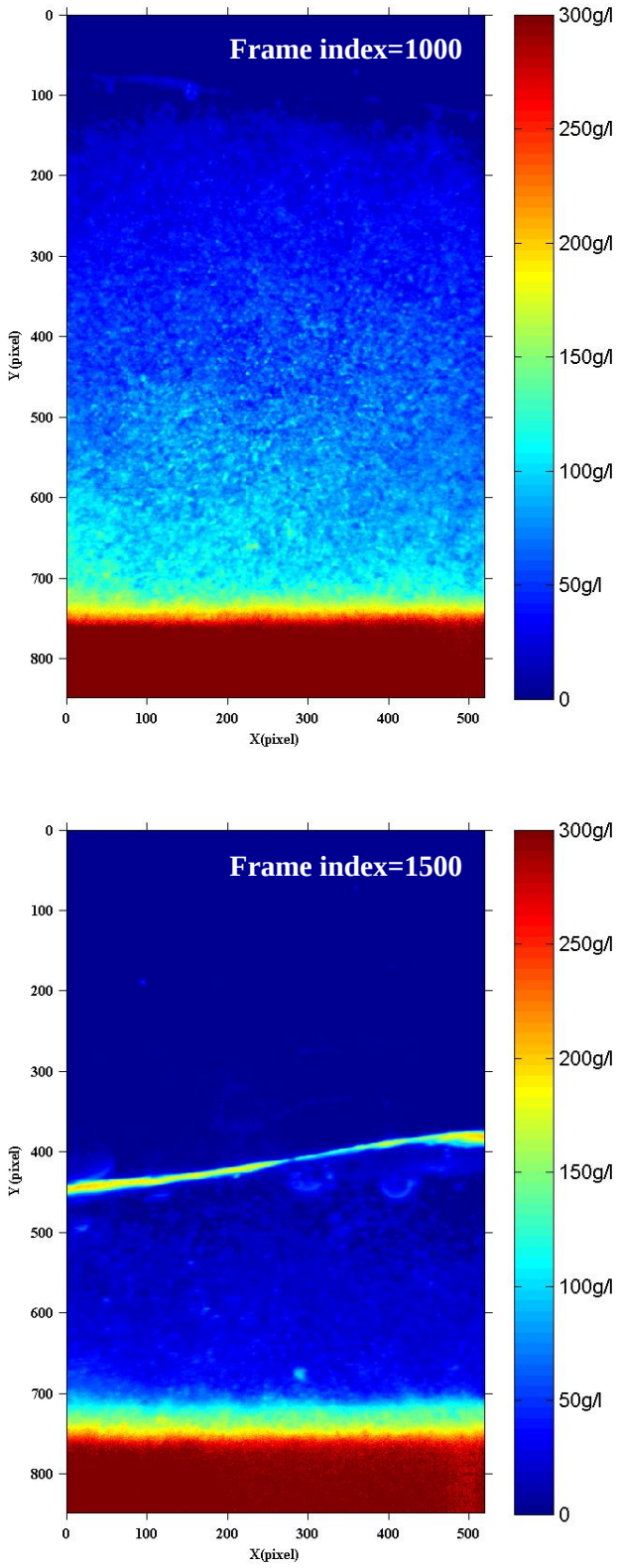

Figure 4-11(2) Example images of concentration distribution

4.3 Experimental results

4.3.1 Bed form variation

The sand bed was underwent 20 dam-break waves in total. Variation of the bed profile was increasingly great because the bed was not rebuilt after each wave. Fig. 4-12 presents the initial bed form and the bed profile after 5 waves, 10 waves and 20 waves test. The net cross-shore sediment transport is more conspicuous under early waves than latter. The change of the initial profile slowed down and turned out to be not proportional to the number of dam-break waves. In addition, it did not achieve equilibrium even until 20 waves washing.

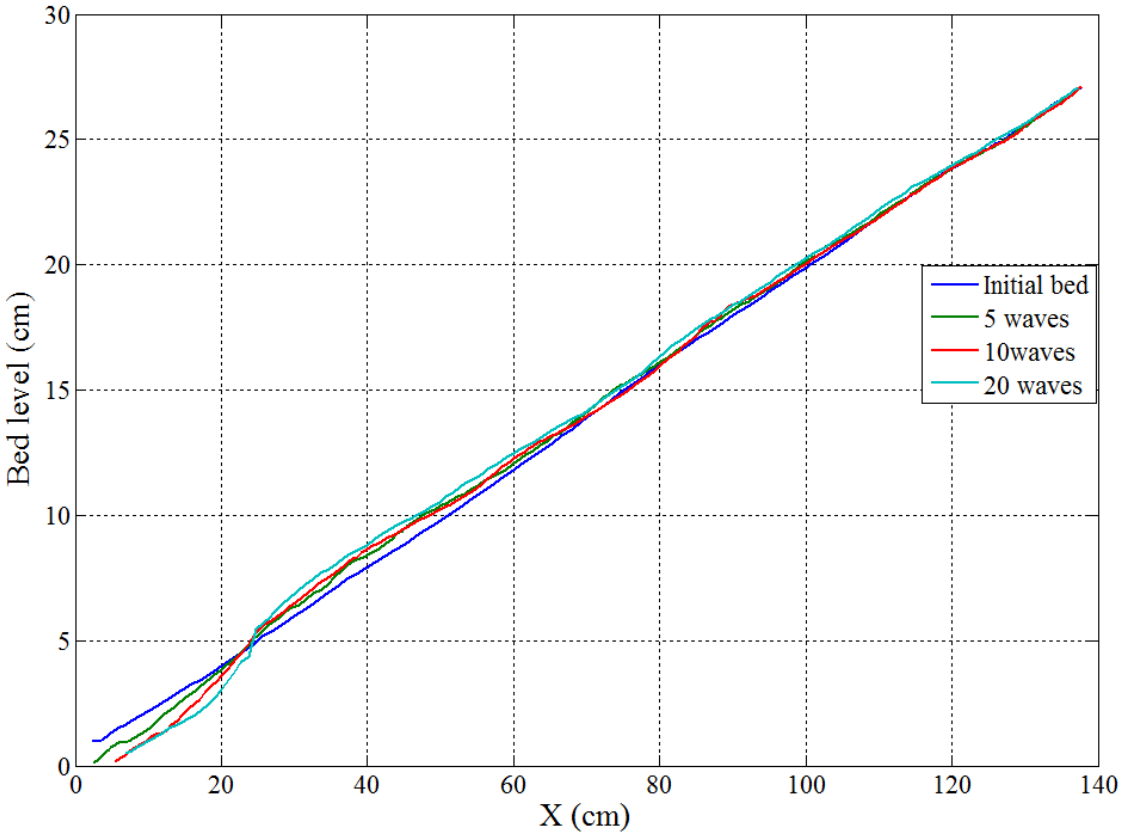

Figure 4-12 Temporal variation of bed profile

The intersection point of erosion and deposition is located about 25 cm from the toe of the bed, and it did not change much among the 20 waves. The erosion zone is located at x < 25 cm. This part of sediment was picked up by waves and finally deposited on the upper bed. The vertical accretion depth was growing but the speed of change was smaller than the erosion. It should be noted that the bed profile very close to the toe of the slope was not measured successfully. Because this part of sand was under SWL (still

water level), and the vertical laser sensor was unable to measure distance when water exists.

4.3.2 Variation of transport velocity and sediment concentration

The 20 dam-break waves were exactly similar, so only one of the analyzed results will be presented in the following. As mentioned above, high spatial and temporal distribution of sand particle velocity distribution is achieved successfully based on the enhanced PIV technique. In addition, distribution of sediment concentration is also obtained through the light extinction method. Fig. 4-13 illuminated the temporal distribution of horizontal and vertical velocities at four different levels from 2 mm above the initial bed level to 30 mm above the initial bed level at inspection line 2 (the left-most inspection line in Fig. 4-10 is defined as the inspection line 1, second line on the left is defined as the inspection line 2, and so on). Wave run-up and run-down lasts longer close to the bed and the duration decreases with the increase of elevation. Wave run-up just continues for 0.75 s in the elevation of 2 mm above the initial bed, while the wave run-down is much longer, reaching 1.6 s. Velocities in the very beginning of uprush is significantly fast, which can be as large as 80 cm/s, while velocities in the final stage of down rush is slightly smaller than 80 cm/s because of energy loss due to friction, just around 70 cm/s. Large velocity fluctuation appears both in the very initial stage of run up and final stage of rush down. Air bubbles bring errors to the velocity analysis at the very beginning of run up, which is a ubiquitous problem in turbulent conditions. In the final stage of wave rushing down, water level changes moment by moment. When the water level is above the interrogation position, velocities can be measured probably. Otherwise, when the water level is below the interrogation position,

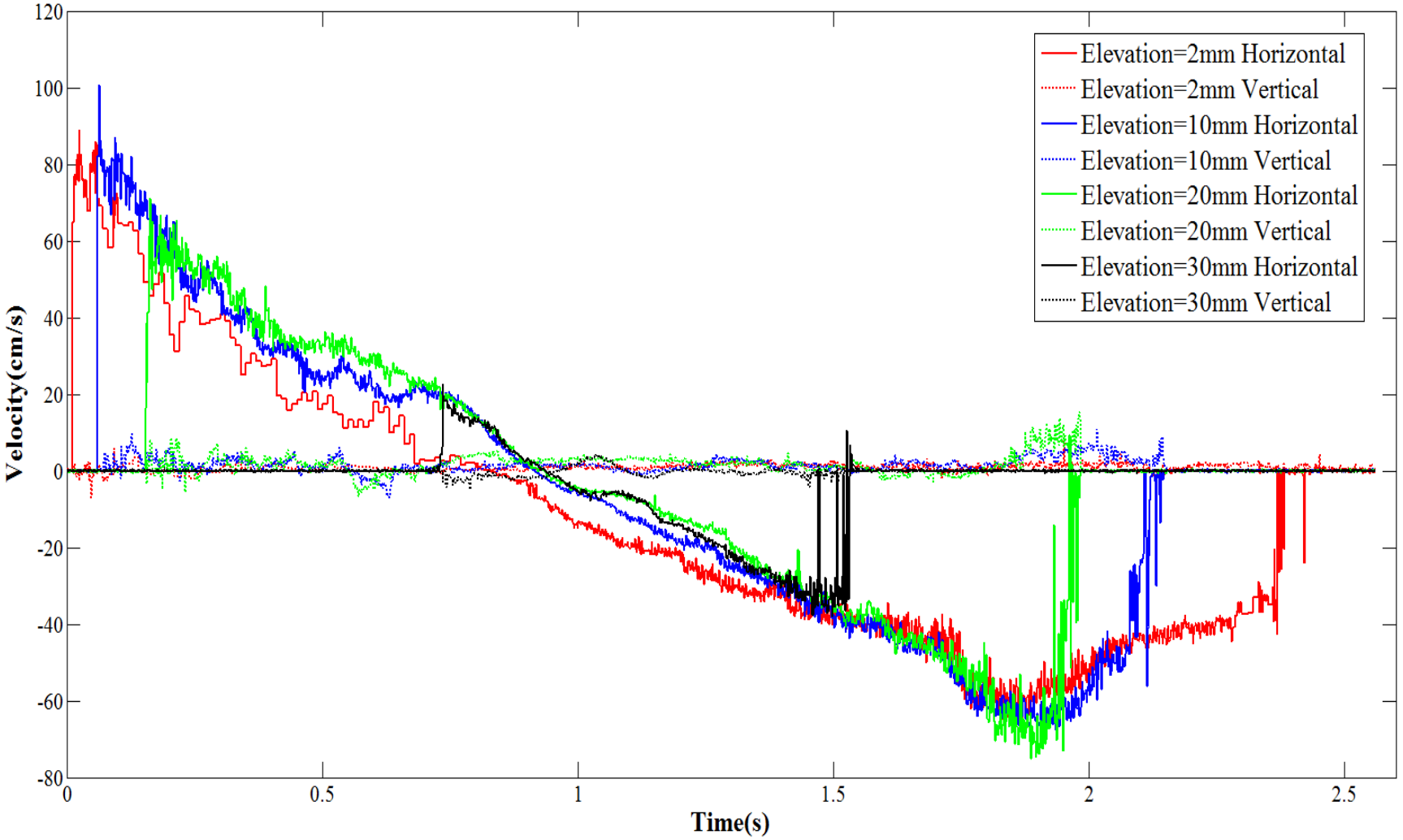

Figure 4-13 Temporal distribution of horizontal and vertical velocity

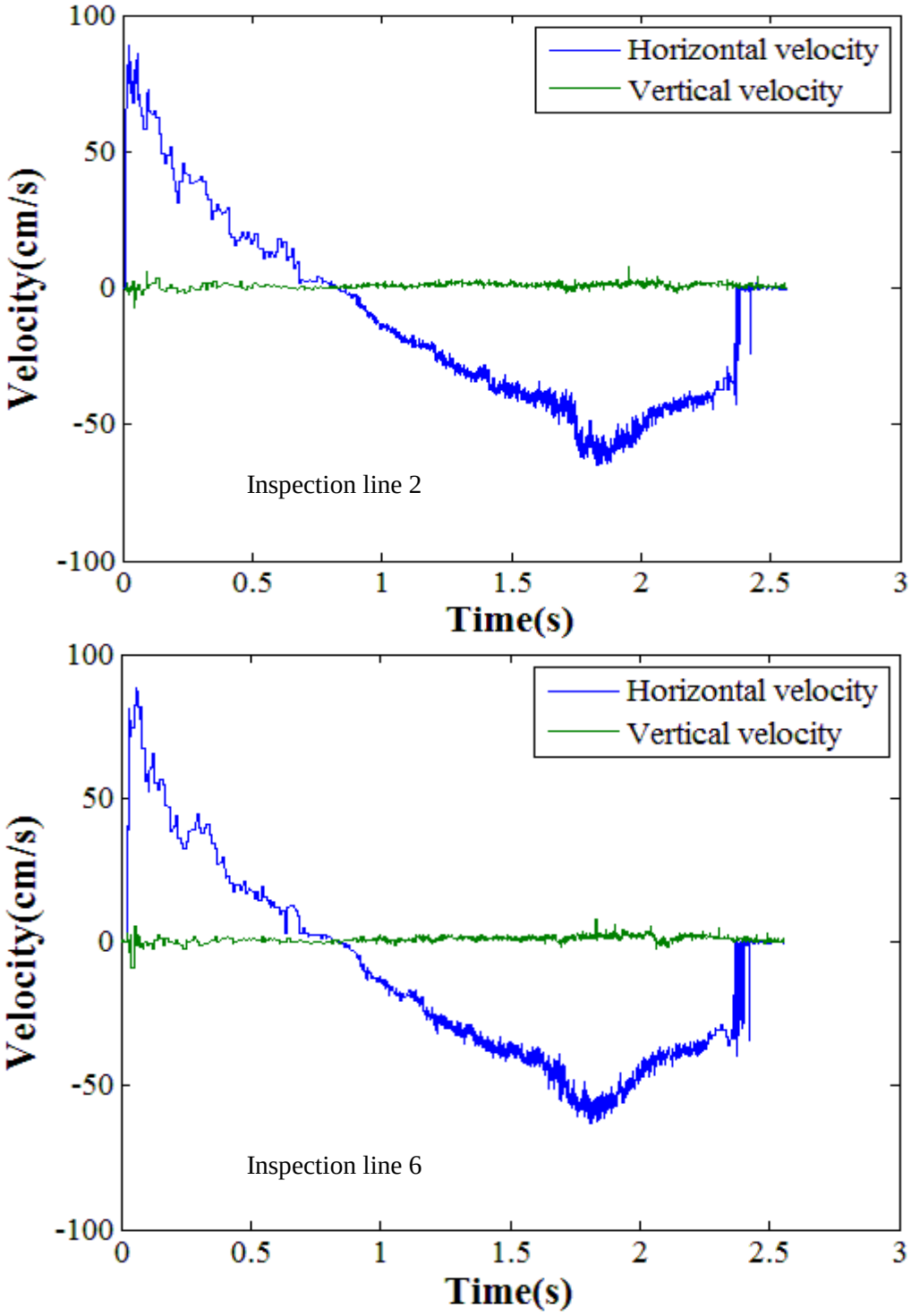

Figure 4-14 (a) Temporal velocity variation at different inspection lines

velocities cannot be measured. Moreover, even the free surface is above the interrogation point, it is most likely failed to obtain velocities as there are no sediment

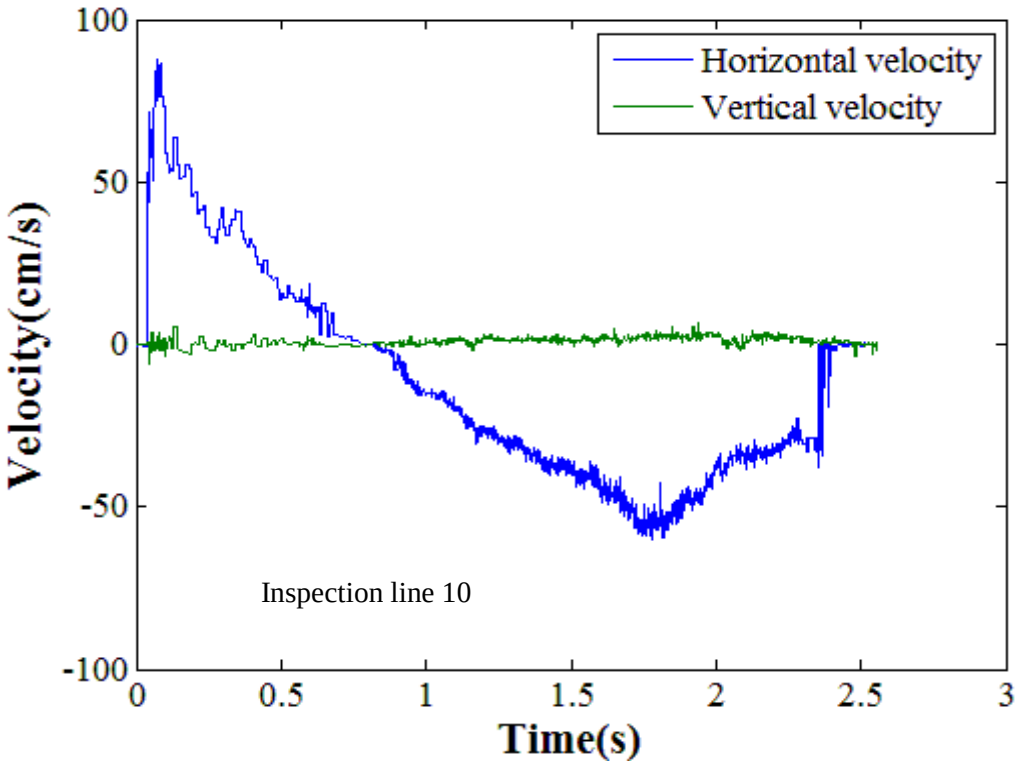

Figure 4-14 (b) Temporal velocity variation at different inspection lines

particles or not enough particles close to the water surface. And sometimes the free surface is in the middle of the interrogation window, which means that the interrogation widow contains both athletic concentrated flow and motionless EL-sheet. This also leads to inaccuracy when doing PIV analysis. Fig. 4-14 shows the temporal velocity variation in the elevation of 2 mm above the initial bed at the inspection line 2, 6, 10 respectively. Similar tendency of velocity distributions also illustrated that the enhanced PIV technique is quite reliable.

Fig. 4-15 shows the vertical distribution of horizontal velocity at inspection line of 2 and 10 from 2 mm below the initial bed level to 12 mm above the initial bed level at different phases (from 0.08 s to 2.28 s). The velocity profiles show the existence of logarithmic layer during the up-wash and down-rush stages. The vertical profile of horizontal velocity has a typical ‘forward leaning’ shape. And it is obvious that in the

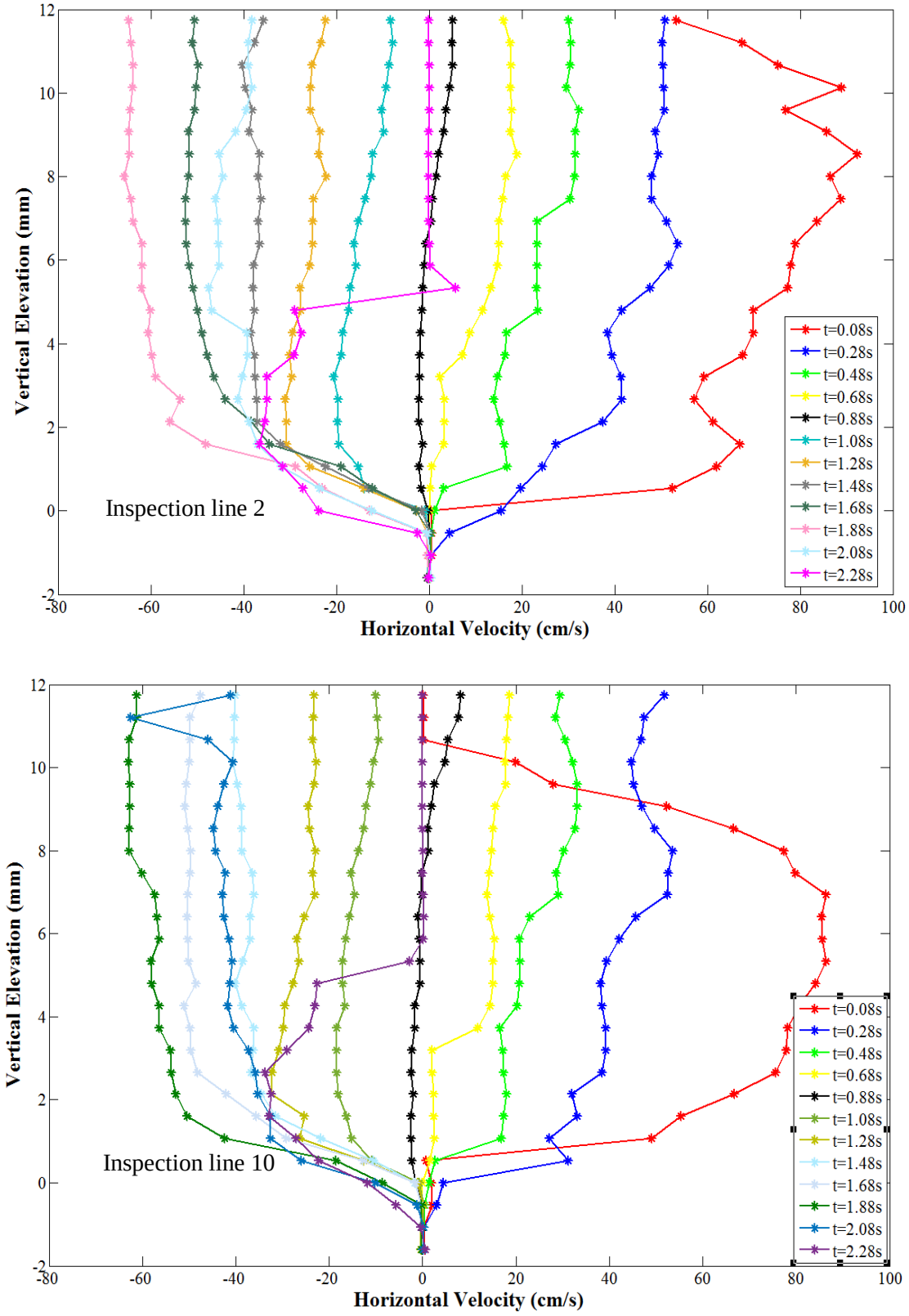

Figure 4-15 Horizontal velocity distribution at different phases

very beginning of the wave run up the velocity gradient is largest and it decays until the flow starts to go reverse. The velocity profile turns to be ‘backward leaning’ shape and velocity gradients keeps growing in the stage of down rush, while it decreases again in the final stage of down rush.

Fig. 4-16 shows the temporal variation of sediment concentration from 2 mm above the initial bed to 30 mm above the initial bed at different inspection lines. When the dam-break wave comes, sediment concentration reaches a peak rapidly, and then it keeps falling even when the flow starts to go reversal. And another peak appears in the final stage of back rush. However, this is caused by the uneven water surface in the direction perpendicular to the EL-sheet and the side wall. In this condition, light attenuation is particularly larger than normal as the space between the side wall and the EL-sheet is not filled with water (Fig. 4-3 (b)). Ant it should be noted that at the elevation of 2 mm above the initial bed, the concentration actually increased because the free surface decreased quickly and suspended sediments at high elevations assemble sharply in the final stage of rush down. So the former increase part of the second peak at the elevation of 2 mm above the initial bed is regarded as credible while the later sharp peak and the other sharp peaks at higher elevations are considered as measuring error. Sediment concentration close to the bed is much larger than the up layers. Maximum concentration in the elevation of 2 mm above the bed reaches 250 g/l, while it is only around 50 g/l in the elevation of 30 mm above the bed (except the second peak caused by the measuring error). The EL-sheet is about 30 mm from the toe of the bed and it is an accretion region which has been indicated before (Fig. 4-12). Although the down rush period is longer than the up wash period, while the region where the EL-sheet

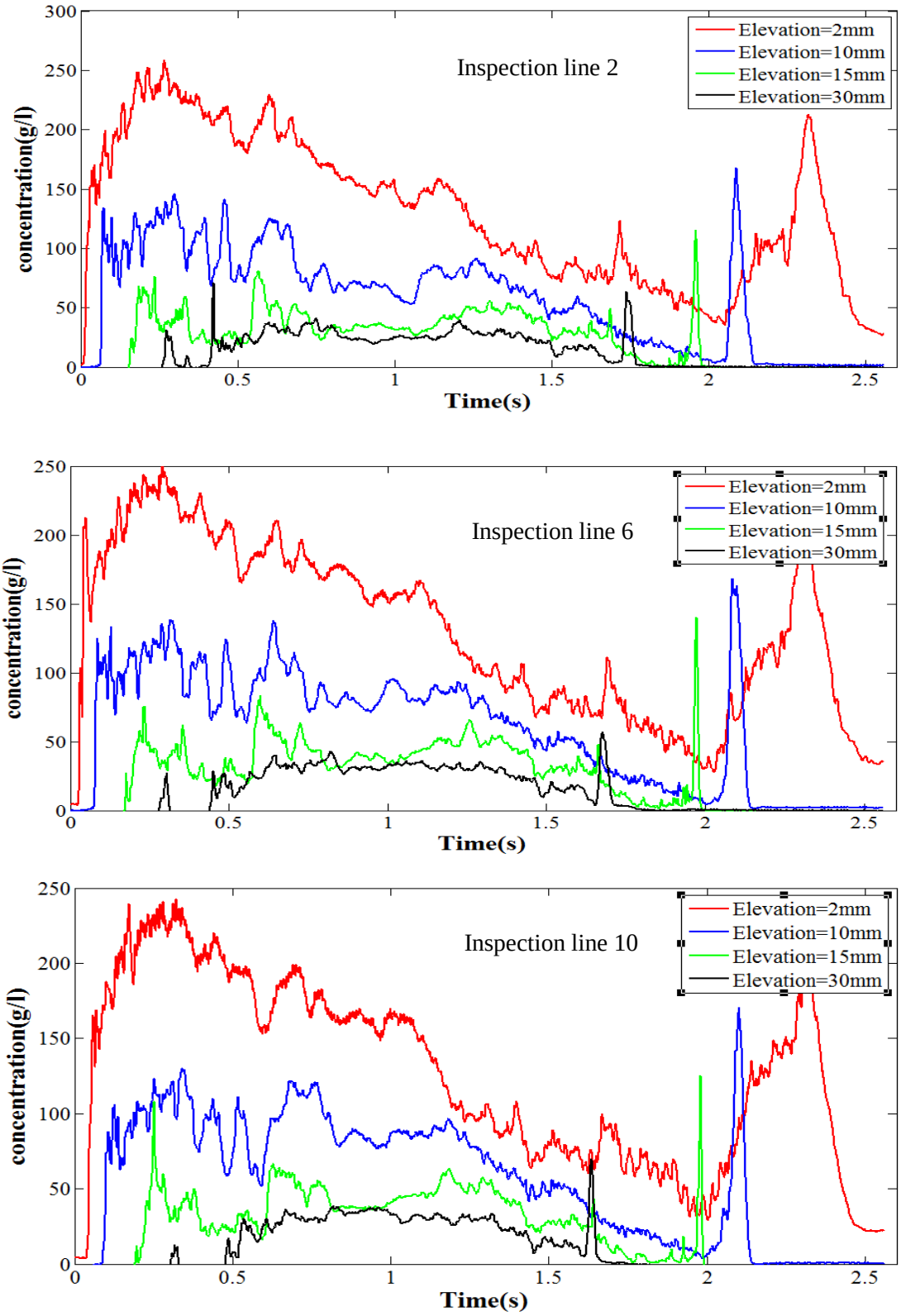

Figure 4-16 Horizontal velocity distribution at different elevations

installed is accreted. The reason can be explained like this, transport velocity and sediment concentration during the up rush period are much larger than those in the down rush, and it offsets the effect of longer wave rush down process.

Fig. 4-17 shows the time series of measured sediment concentrations and velocities at different elevations in inspection line 2. At the elevation of 2 mm above the initial bed, when dam-break wave collapsed on the sand bed, a large budget of sediment was suspended due the huge wave force, which results in a sudden increase of sediment concentration. And then sediment concentration kept decreasing undulated until the final stage of the wave rush down. As the free surface decreased rapidly, large vertical velocities made the sediment particles aggregate quickly in the thin water layer, which leads to the concentration increased again. This phenomenon is not obvious at the elevation of 10 mm above the initial bed. At this elevation, after a sudden increase of sediment concentration, the concentration fluctuated significantly. At the elevation of 20 mm above the bed, sediment concentration kept relatively stable for about 0.5 s after a fluctuation period. Because at this elevation, the flow was relatively steady and sediment particles were almost homogeneously in the whole flow field at the later stage of wave run up and initial stage of wave rush down, which made the change of concentration kept stable. At the elevation of 30 mm above the initial bed, sediment concentration kept growing with the increase of the free surface after the wave arrived. Because at this elevation, suspended sediments were lifted by the wave force constantly until the free surface reaches highest. And it fell quickly along with the decreasing of the free surface, and there is no further increase appears as the last sharp peak has already been indicated as measuring error. In summary, sediment suspension

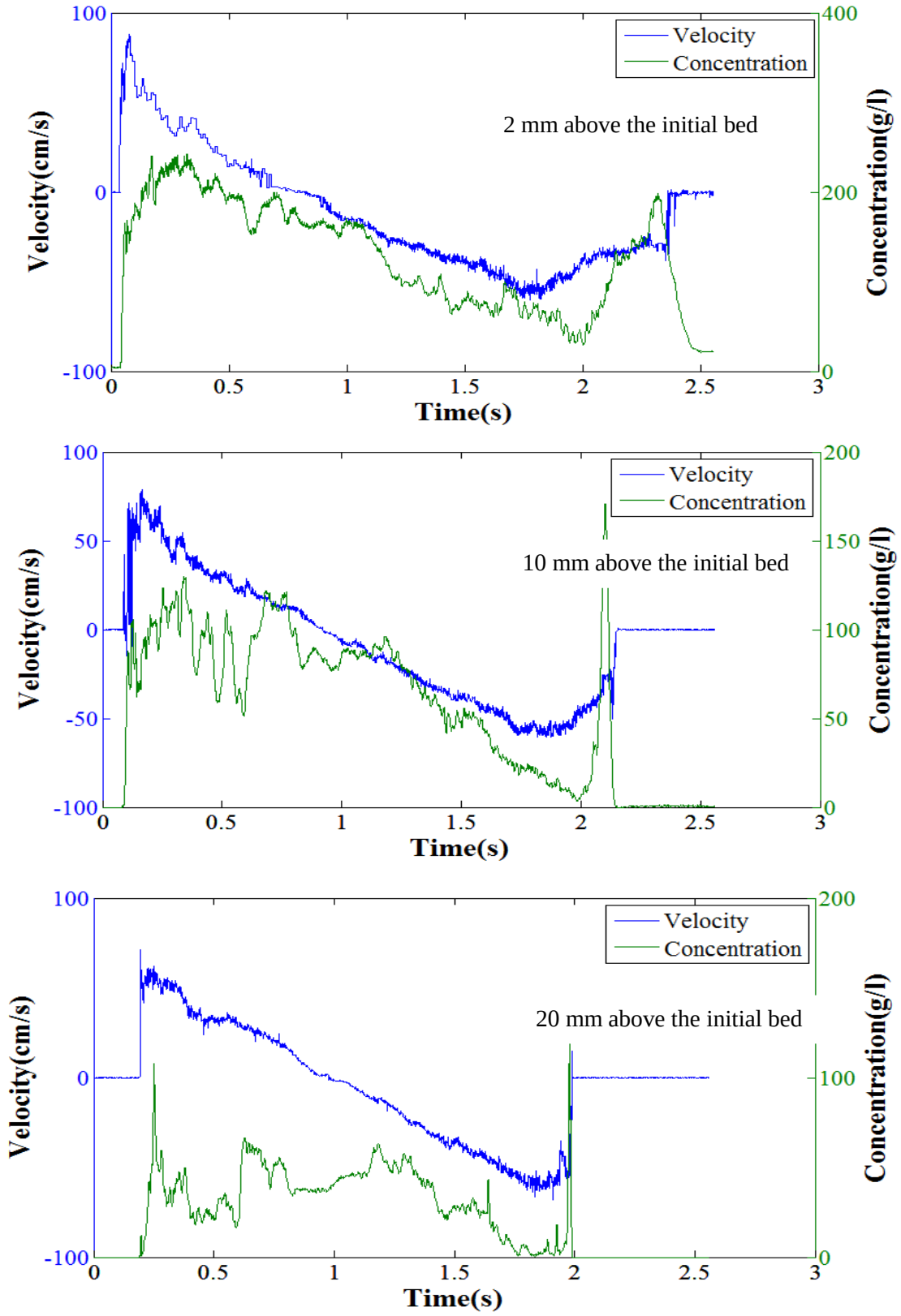

Figure 4-17 (a) Variation of transport velocity and sediment concentration at different elevations

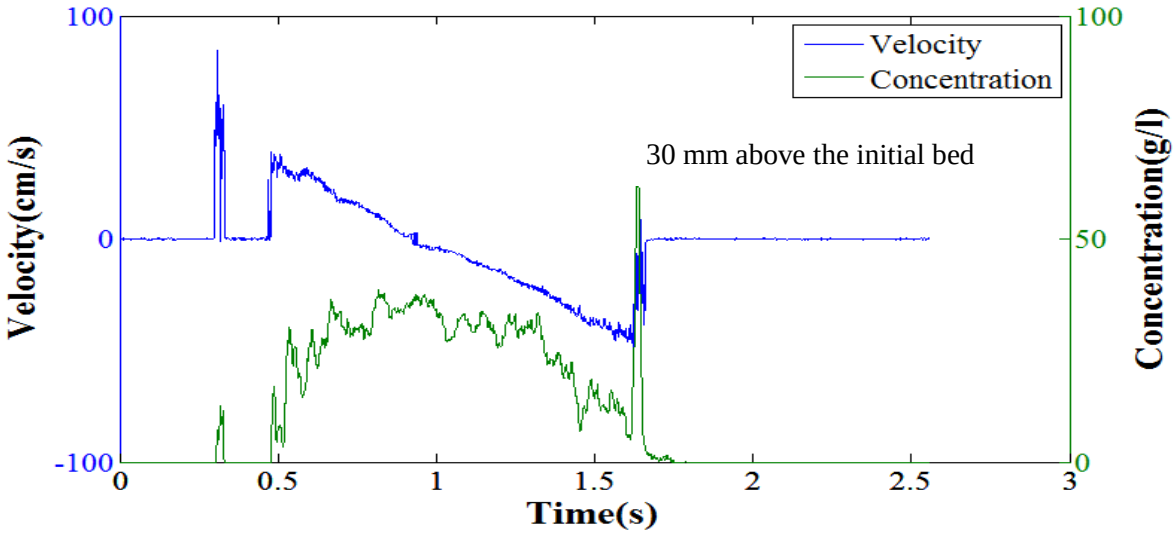

Figure 4-17 (b) Variation of transport velocity and sediment concentration at different elevations

occurs only at the very beginning of the dam-break wave, and characteristics of the transporting sediments are various intensively at different elevations.

4.3.3 Sediment transport rate

Similar with the sediment concentration and transport velocity, sediment transport rate Q was measured at the same spatial and temporal resolution by product the instantaneous transport velocity, u (x, z, t), and sediment concentration, c (x, z, t).

$$Q(x,z,t) = u(x,z,t) \times c(x,z,t) \tag{4-3}$$

Fig. 4-18 shows the temporal variation of sediment transport rates from 2 mm above the initial bed to 30 mm above the initial bed at different inspection lines. Sediment transport rate during wave run up is much larger than that in wave rush down. It corresponds to the fact that net sediment transport is onshore. And sediment transport rate close to the bed is much larger than the upper layers. Tendency of sediment

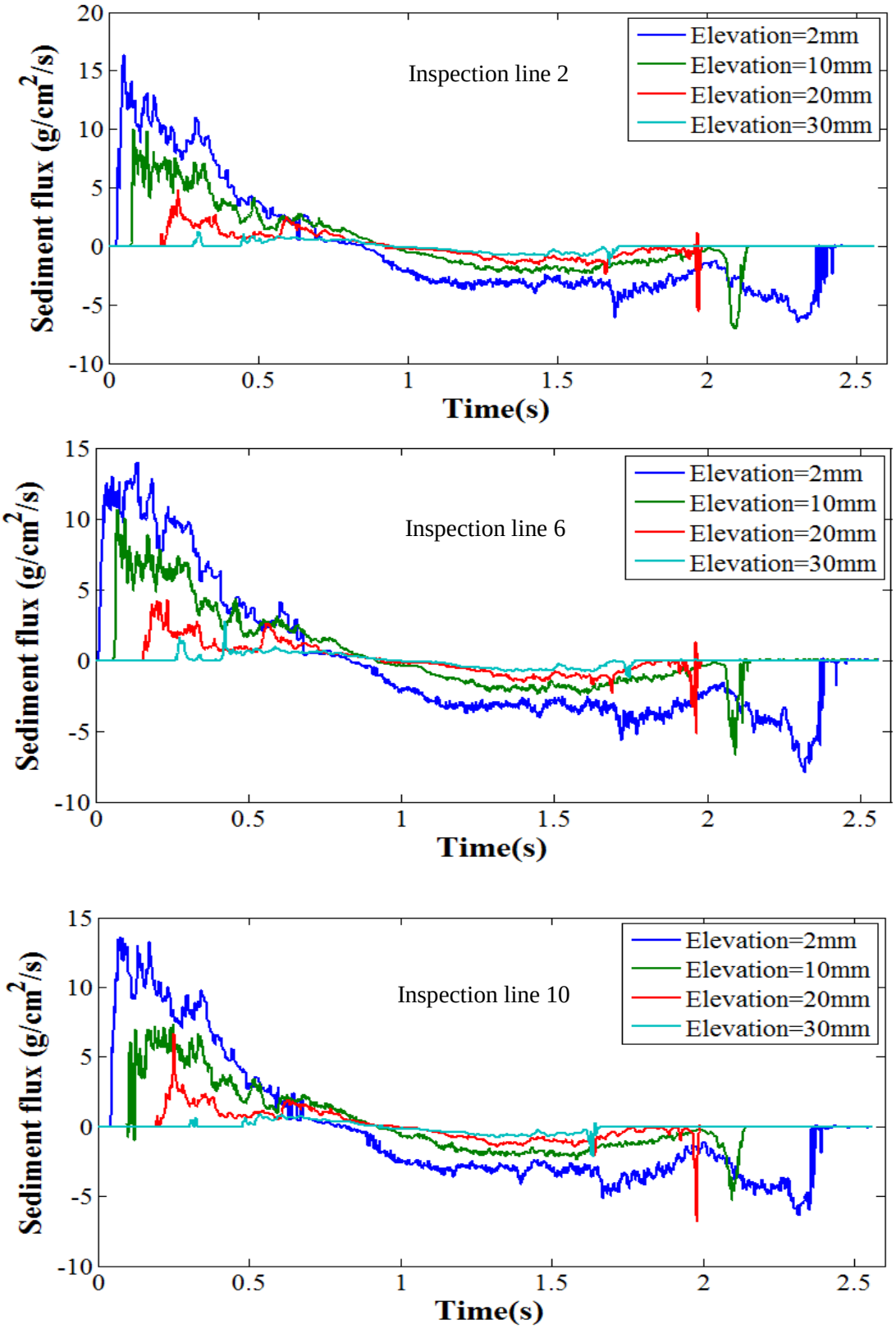

Figure 4-18 Sediment transport rate at different elevations

transport rates among different inspection lines are extremely similar, which also testifies the accuracy and reliability of the current measurement technique.

In order to analysis the relationships among the sediment transport rate, transport velocity and sediment concentration, these three factors at different elevations are plotted in the same figure (Fig. 4-19). At the elevation of 2 mm above the initial bed, sediment transport rate reached a peak as soon as the dam-break wave front arrived at the bed. Then it kept decreasing even though the sediment concentration was fluctuating significantly. When the flow went reverse, sediment transport rate remained stable for about 1 s companied with the constantly growing velocity and fluctuated decreasing concentration. At the final stage of wave rush down, sediment concentration went up rapidly, which results in the increase of transport rate although transport velocity was decreasing during that period. At the elevation of 10 mm above the initial bed, sediment concentration fluctuated violently in the stage of wave run up, while sediment transport rate kept decreasing with the continuously falling velocity. During the wave rush down, concentration dropped quickly but sediment transport rate declined more slowly due to the increasing transport velocity. In the further upper layers, sediment transport rates were significantly smaller than the low layers. Transport rate followed the fluctuation of sediment concentration well and it turned to be almost zero in the final stage of wave rush down.

Under the combination influence of sediment concentration and transport velocity, sediment transport rate also varies hugely at different elevations and phases. Whereas the fluctuation of transport rate is not as significant as the change of sediment concentration, and sediment transport close to bed dominants the change of bed profile.

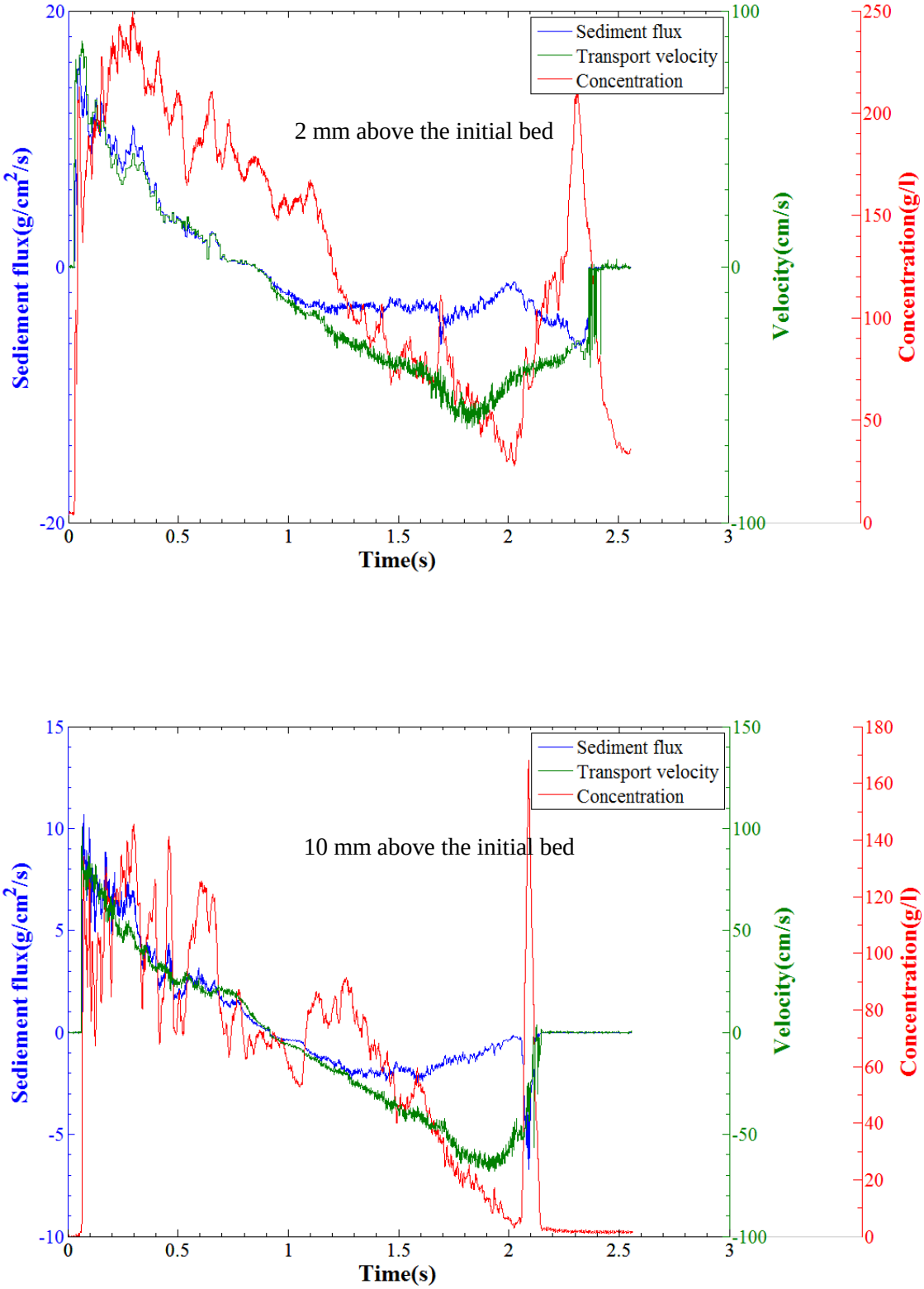

Figure 4-19 (a) Variation of sediment transport rate, transport velocity and sediment concentration at different elevations

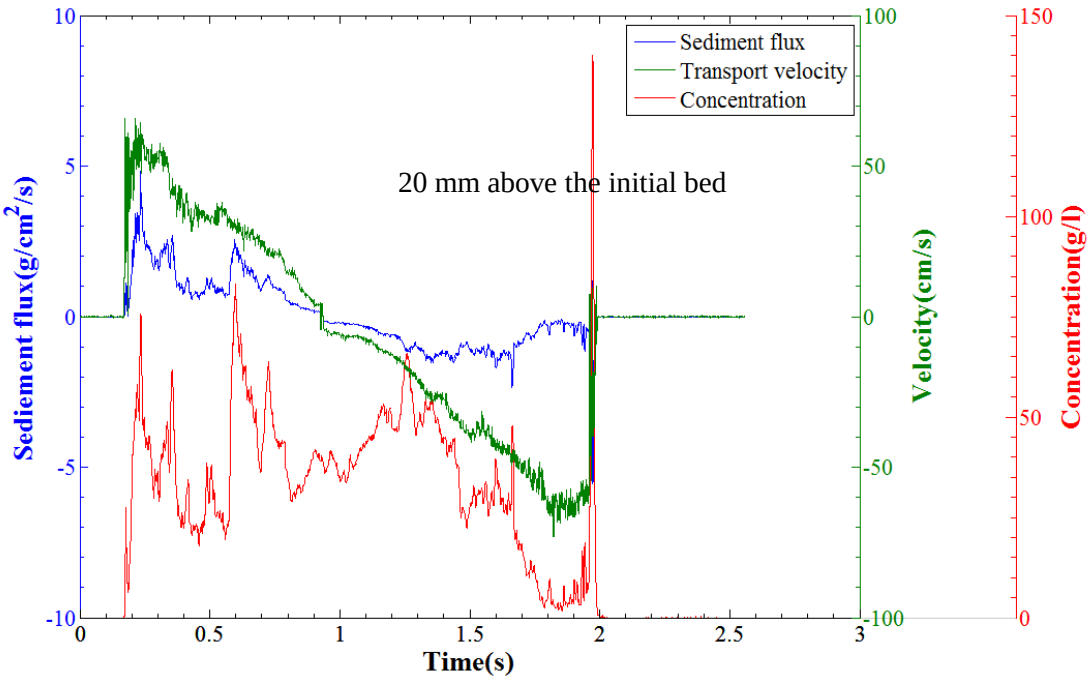

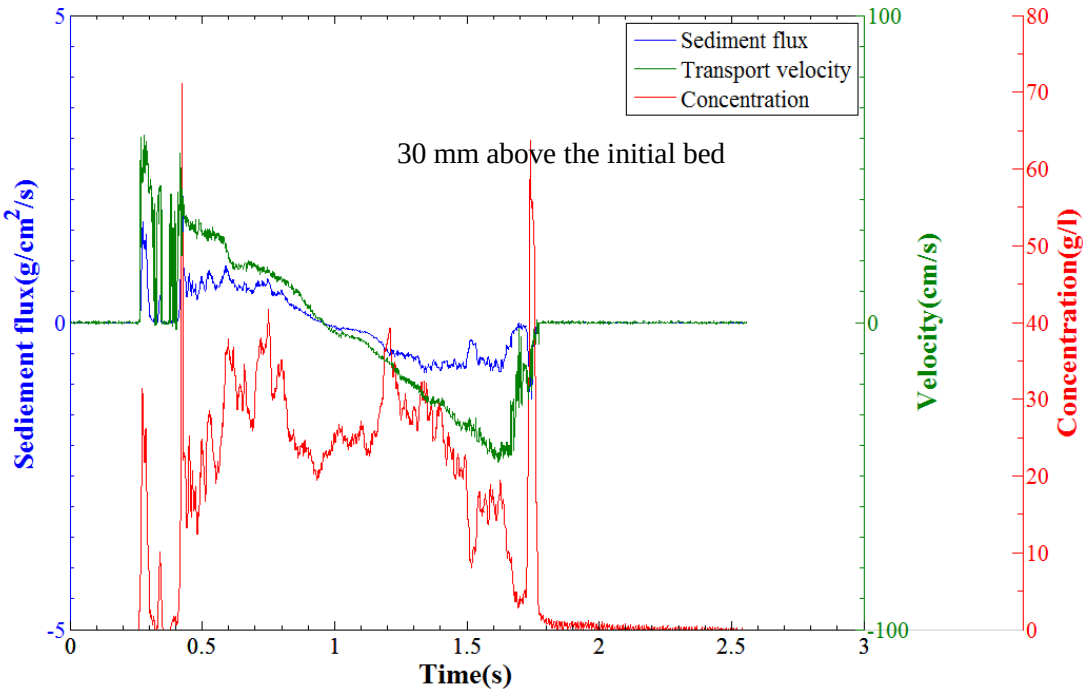

Figure 4-19 (b) Variation of sediment transport rate, transport velocity and sediment concentration at different elevations

Charpter5. Conclusions and recommendations

An improved measurement system was developed to quantify the sediment flux depends on two image-based techniques for sediment concentration and velocity measurement respectively. Sediment concentration measurement based on the light extinction method shows good reliability. Calibration for sediment concentration measurement was carried out under a series of conditions, and measuring range for each path length was clarified. Transported velocity measurement under dense conditions was achieved by enhanced PIV technique with the help of an additional light source, stroboscope. Measuring range of the existing sediment flux measurement system was further confirmed. It was found that the factor of light attenuation in 2.5 is the measuring limit of the previous system. Verification tests for the improved sediment transport measurement system were carried out. The results suggest that limitation in the factor of light attenuation has been broken through in the improved system, and the system is capable of measuring sediment concentration over 190 g/L with an error no more than 10% in the path length of 1.5 cm and it is not the measuring limit.

Laboratory experiment of sediment transport measurement was carried out in an open channel flume under dam-break bores based on the improved measurement system. Sediment transport is onshore. Bottom of the bed was eroded more and more seriously with the increase of dam-break wave number. The erosion area is much narrower than the accretion section. The intersection is about 25 cm from the toe of the bed. Change of the bed profile slowed down while it did not achieve a balance even after 20 dam-break waves.

Sediment concentration close to the bed is much larger than the up layers and it decreased with the increase of elevation. Sediment suspension appears only at the initial stage of wave collapsing and characteristic of sediment concentration at different elevations are remarkably different. In the final stage of wave down rush, large error of concentration measurement occurs due to the influence of the free surface. Further post processing is expected to be developed for avoiding the influence of free surface and air bubbles, and increasing the accuracy of sediment concentration measurement in the final stage.

Sediment transport velocities with high resolution and accuracy were obtained by employing the advanced PIV technique. Transported velocity decreased rapidly after the wave collapsing on the bed. And then it increased constantly with the wave running down until the final stage of down rush where the velocity decreased slightly again. Velocity fluctuation in the initial stage of up wash final stage of down rush is significant due to the influence of changeful free surface and air bubbles, which is one of the shortages of the current study. The vertical profile of horizontal velocity has a typical ‘forward leaning’ shape. And it is obvious in the very beginning of the wave run up and then the velocity gradients decays until the flow starts to go reverse. The velocity profile turns to ‘backward leaning’ shape and velocity gradients keeps growing in the stage of down rush, while it decreases again in the final stage of down rush.

Sediment transport rate close to the bed is also much larger than the up layers. The fluctuation of temporal variation of sediment transport rate is much smaller compared with sediment concentration change. Transport rate varies significantly at different elevations as well, and the sediment transport close to bed dominants the bed transform.

In current study, sediment concentration, transport velocity and sediment transport rate are only analyzed at elevations of 2 mm, 10 mm, 20 mm, and 30 mm above the initial bed. And numerous conclusions have been proposed based on the temporal variation of velocity and concentration at these elevations. While in order to understand the mechanisms for the difference among different elevations, more detailed analysis for wider elevations are necessary.

Some other factors such as turbulent intensity and bed shear stress are also expected to be analyzed for making deeper insight into the boundary layer structure of moveable bed. Moreover, net sediment transport rate is expected to be associated with the change of bed profile by further analysis.

REFRENCE

1. Agrawal, Y.C., Pottsmith, H.C., 1993. Optimising the kernel for laser diffraction particle sizing. Applied Optics 32 (22), pp.4285–4286.
2. Agrawal, Y.C., Pottsmith, H.C., 1994. Laser diffraction particle sizing in STRESS. Continental Shelf Research 14 (10/11), pp.1101–1121.
3. Agrawal, Y.C., Pottsmith, H.C., 2000. Instruments for particle size and settling velocity observations in sediment transport. Marine Geology 168, pp.89–114.
4. Berke, B. and Racoczi, L., 1981. Latest achievements in the development of nuclear suspended sediment gauges. Proc., Erosion and Sediment Transport Measurement (Symp.), International Association of Hydrological Sciences, Wallingford, U.K., 91-96
5. Bothner, M.H. and Valentine, P.C., 1982. A New Instrument for Sampling Flocculent Material at the Water/Sediment Interface. Journal of Sedimentary Petrology, 52 (2) pp.639-640
6. Bunt, J.A.C., Larcombe, P., Jago, C.F., 1999. Quantifying the response of optical backscatter devices and transmissometers to variations in suspended particular matter. Continental Shelf Research 19, pp.1199-1220
7. Conner, C.S. and Devisser, A.M., 1992. A laboratory investigation of particle size effects on an optical backscatterance sensor. Marine Geology 10, pp.151-159
8. Dark, P. and Allen, J.R.L., 2005. Seasonal deposition of Holocene banded sediments in the Severn Estuary Levels (southwest Britain): palynological and sedimentological evidence.

9. Dick, J.E., Sleath, J.F.A., 1991. Velocities and concentrations in oscillatory flow over beds of sediment. Journal of Fluid Mechanics 233, pp.165 – 196
10. Dick, J.E., Sleath, J.F.A., 1992. Sediment transport in oscillatory sheet flow. Journal of Geophysical Research 97, pp.5745-5758
11. Downing, J., 2006. Twenty-five years with OBS sensors: The good, the bad and the ugly. Continental Shelf Research 26, pp.2299-2318
12. Downing, J., Sternberg, R.W., Lister, C.R.B., 1981. New instrumentation for investigation of sediment suspension in the shallow marine environment. Marine Geology 42, pp.19–34.
13. Downing, J.P., Sternberg, R.W., Lister, C.R.B., 1981. New instrumentation for the investigation of sediment suspension processes in the shallow marine environment. Marine Geology 42, pp.19-34
14. Hanes, D.M., Vincent, C.E., Huntley, D.A., Clarke, T.L., 1988. Acoustic measurements of suspended sand concentration in the C^2S^2 experiment at Stanhope Land, Prince Edwards Island. Marine Geology 81, pp.185-196
15. Hay, A. E., Wilson, D., 1992. Vertical profiles of suspended sand concentration and size from multifrequency acoustic backscatter. Journal of Geophysical Research 97 (C10), 15661-15677
16. Keane R.D., Adrian, R.J., 1992. Theory of cross-correlation of PIV images, Applied Scientific Research, Vol.49, pp. 191-215
17. Kiyoshi, H., 1988. Nearshore dynamics and coastal process. Japan, University of Tokyo Press, pp.136-137.
18. Lewis, J., 1996. Turbidity-controlled suspended sediment sampling for runoff-event load estimation. Water Resources Research, 32(7), pp.2299-2310

19. Libicki, C., Bedford, K.W., Lynch, J.F., 1989. The interpretation and evaluation of a 3-MHz acoustic backscatter device for measuring benthic boundary layer sediment dynamics. Journal of the Acoustical Society of America, Vol. 85, No. 4 pp.1501–1511
20. Liu, H. and Sato, 2005. Laboratory study on sheetflow sediment movement in the oscillatory turbulent boundary layer based on image analysis, Coastal Eng. Journal 47(1), pp.21-40
21. Liu, H. and Sato, S.: Laboratory study on sheetflow sediment movement in the oscillatory turbulent boundary layer based on image analysis, Coastal Eng. Journal, Vol.47(1), pp.21-40, 2005.
22. Longo, S., Petti, M., Losada, I. J., 2002. Turbulence in the swash and surf zones: a review. Coastal Engineering 45, pp.129-147
23. Ludwig, A.J. and Hanes, D.M., 1990. A laboratory evaluation of optical backscatterance suspended solids sensors exposed to sand-mud mixtures. Marine Geology 94, pp.173-179
24. Ludwig, K.A., Hanes, D.M., 1990. A laboratory evaluation of optical backscatterance suspended solids sensors exposed to sand-mud mixtures. Marine Geology 94, pp.173–179
25. Lynch, J.F., Gross, T.F., Brumley, B.H., Filyo, R.A., 1991. Sediment concentration in HEBBLE using a 1-MHz acoustic backscatter system. Marine Geology 99, pp.361–385.
26. Masame, Y., 2013. Image based technique for sediment flux measurement with a light transmission method (In Japanese). Mater thesis, Tokyo University of Marine Science and Technology

27. Masselink, G. and Kroon, A., 2009. Coastal zone and estuaries. EOLSS, pp.221-223
28. Masselink, G. and Puleb, J.A., 2006. Swash-zone morphodynamics. Continental Shelf Research 26, 661-680.
29. Mimura, N. etc., 2000. Design manual for coastal facilities. JSCE, 134pp.
30. O'Donoghue, T., Wright, S., 2004. Flow tunnel measurements of velocities and sand flux in oscillatory sheet flow for well-sorted and graded sands. Coastal Engineering 51, pp.1163-1184

    Quaternary Science Reviews, 24 (1-2), pp.11-33
31. Radice, A., Malavasi, S., Ballio, F., 2006. Solid transport measurements through image processing, Exp. Fluids, Vol.41 pp.721-734
32. Raffel, M., C. E. Willert, and J. Compenhans, 2007. Particle Image Velocimetry: A Practical Guide, Springer, Berlin Heidelberg New York
33. Ribberink, J.S., Al-Salem, A.A., 1995. Sheet flow and suspension of sand in oscillatory boundary layers. Coastal Engineering 25, pp.205 – 225
34. Shimozono, T., Masame, Y. and Okayasu, A., 2013. Image-based measurement of sediment flux for highly concentrated sediment-laden flows. Journal of JSCE 69(2), pp.1426-1430
35. Shimozono, T., Masame, Y., Kobayashi, K. and Okayasu, A., 2012. Light-transmission planar measurement of sediment flux under water flow. Japanese J. Multiphase Flow 25(5), pp.435-442
36. Shimozono, T., Masame, Y., Okayasu, A.: Image-based measurement of sediment flux for highly concentrated sediment-laden flows, Journal of JSCE, Vol.69(2) , 2013.

37. Shimozono, T., Sasaki, A., Okayasu, A., Matsubayashi, Y., 2008. Laboratory measurement of high sediment concentration with light extinction method, Journal of JSCE 55, pp.1436-1440
38. Sternberg, R.W., Kineke, G.C., Johnson, R., 1991. An instrument system for profiling suspended sediment, fluid and flow conditions in shallow marine environments. Continental Shelf Research 11, pp.109–122
39. Syvitski, J.P.M., Vorosmarty, C.J., Kettner, A.J. and Green, P., 2005. Impact of humans on the flux of terrestrial sediment to the global coastal ocean. Science, 308 (5720):376-380.
40. Thorne, P.D., and Hanes, D.M., 2002. A review of acoustic measurement of small-scale sediment process. Continental Shelf Research, 22, pp.603-632
41. Thorne, P.D., Hardcastle, P.J., 1997. Acoustic measurements of suspended sediments in turbulent currents and comparison with in-situ samples. Journal of the Acoustical Society of America, 108 (4), 1568-1581
42. Thorne, P.D., Hardcastle, P.J., Soulsby, R.L., 1993. Analysis of acoustic measurements of suspended sediments. Journal of the Geophysical Research 98 (C1), pp.899-910
43. Thorne, P.D., Holdsaway, G.P., Hardcastle, P.J., 1995B. Constraining acoustic backscatter estimates of suspended sediment concentration profiles using the bed echo. Journal of the Acoustical Society of America 98 (4), pp.2280-2288
44. Thosteson, E.D., Hanes, D.M., 1998. A simplified method for determining sediment size and concentration from multiple frequency acoustic backscatter measurements. Journal of the Acoustical Society of America, 104 (2)(Pt.1), pp.820-830

45. Traykovski, P., Hay, A.E., Irish, J.D., Lynch, J.F., 1999. Geometry, migration, and evolution of wave orbital ripples at LEO-15. Journal of Geophysical Research 104 (C1), pp.1505–1524

46. Westerweel,J. and Scarano, F., 2005. Universal outlier detection for PIV data. Experiments in Fluids 39, pp.1096-1100

47. Wren, D., Barkdoll, B., Kuhnle, R., and Derrow, R., 2000. Field Techniques for Suspended-Sediment Measurement, Journal of Hydraulic Engineering 126 (2), pp.97-104

48. Yang, S.L., LI, H., Ysebaert, T., Bouma, T.J., Zhang, W.X., Wang, Y.Y., Li, P., Ding, P.X., 2008. Spatial and temporal variations in sediment grain size in tidal wetlands, Yangtze Delta: On the role of physical and biotic controls. Estuarine, Coastal and Shelf Science, 77 (4), pp.657-671